



# Characterization of the Unsteady Wake Aerodynamics for an Industry Relevant Road Vehicle Geometry Using LES

Faron Hesse<sup>1</sup> · Aimee S. Morgans<sup>1</sup>

Received: 3 September 2022 / Accepted: 21 January 2023 / Published online: 7 February 2023  
© The Author(s) 2023

## Abstract

A wall-resolved large eddy simulation (WRLES) study of the flow around a 15% scale model of the Nissan NDP, an electric concept vehicle developed by Nissan, at  $Re_H = 100,000$  is presented. First, wake asymmetries and the associated possibility of wake bimodality occurring are investigated by comparing the flow fields around “square-back” and cavity variants of the Nissan NDP. It is highlighted that there is no noteworthy long-term wake asymmetry in the spanwise direction for both configurations and that there is, instead, symmetric spanwise vortex shedding, as highlighted through the use of proper orthogonal decomposition (POD) post-processing. One can, therefore, exclude the existence of classical wake bimodality in the spanwise direction that has been observed for the Ahmed body. However, the wake does explore the vehicle’s rear space in the spanwise direction rapidly over non-dimensional time intervals of  $\mathcal{O}(10)$ . Meanwhile, there is a strong wake tilt in the vertical direction due to the presence of a ground, the vehicle geometry’s vertical asymmetry, and the detachment of a powerful hairpin vortex from the vehicle’s roof. When looking at POD of the flow field in a vertical plane, asymmetric vortex shedding, similar to that observed for the Ahmed body by Hesse and Morgans (2021) in the spanwise plane, is found. This suggests that wake bimodality in the vertical direction could occur for the Nissan NDP—the presented results are not conclusive, as the provided non-dimensional simulation duration of  $t^* \sim 60$  is insufficient for the bimodal phenomenon that occurs at  $t^* \sim 1000$ . Additionally, the discernible impact of having a cavity at the rear of the NDP is to allow the wake to explore a larger vehicle base space (i.e. the wake is able to move more freely). This, coupled to a 5% reduction in rear base area, translates to a drag reduction compared to the “squareback” variant of 13.6%. Second, in a more qualitative analysis of simulation results, the effect of using a moving ground in simulation as compared to a stationary ground is assessed. This is only done for the cavity variant of the Nissan NDP. It is found that, for this vehicle geometry, a stationary ground is associated with the occurrence of low pressure clockwise rotating (when looking into the page of the vertical plane) vortices near the ground caused by the flow deceleration just aft of the vehicle base, where the flow moves from the vehicle under-body toward the wake’s far-field region. The consequence of this flow phenomenon is to simulate a 3.3% higher drag value with the stationary ground simulation as compared to the moving ground simulation. Thus, although the moving ground should be more representative of the real-world, the stationary ground simulation is more conservative in aerodynamic terms and should be used if

developing the NDP vehicle completely digitally using a virtual twin. By over-design, the stationary ground variant namely ensures that the drag key performance indicator (KPI) is met.

**Keywords** Wall-resolved large eddy simulation (WRLES) · Wake asymmetries · Wake bimodality · Vortex shedding · Hairpin vortex · Passive flow control · Moving ground simulation

## 1 Introduction

Since 1970, approximately 80% of transport sector emission increases are due to road vehicles alone (Edenhofer et al. 2014). In light of evermore stringent CO<sub>2</sub> emission regulations from governmental bodies and the need to satisfy new emission testing procedures, such as the Worldwide Harmonised Light Vehicle Test Procedure (WLTP), road vehicle manufacturers are scrambling to find ways to lower the carbon footprint of their vehicles. Avenues include the development of new efficient engines as well as transmission systems with a particular focus on the gearbox. A further approach is to focus on the vehicle's shape and the resulting aerodynamics.

A large percentage of road vehicles, such as light good vehicles, lorries and even SUVs, can be characterized aerodynamically as blunt bluff-bodies with under-body geometries in close proximity to the road. They are surrounded by flow fields associated with a Reynolds number based on body height,  $Re_H$ , of  $\mathcal{O}(10^6)$ . The resulting aerodynamic properties of these vehicle shapes are dominated by the presence of pressure drag. This force is the consequence of large-scale boundary layer separation at the trailing edge(s) of the vehicle that produces the so-called wake, a.k.a. dead water region, directly aft of the separation line (Hucho and Sovran 1993). While numerous studies, such as He et al. (2018), Papoutsis-Kiachagias et al. (2019) and Othmer (2014), have shown that adjoint methods for shape optimization based on a cost function can effectively find low drag and, therefore, energy conserving vehicle configurations, it is not without a proper understanding of the rear wake's topology and dynamics that one can truly hope to find the best vehicle shape for low CO<sub>2</sub> emission and/or largest electric vehicle range.

A comprehensive understanding of the wake's steady-state behavior has been acquired through both experimental and numerical studies. In the experimental domain, the seminal work of Ahmed (1981) and Ahmed et al. (1984) conclusively determined that the time-averaged near wake is composed of a separation bubble while the far-field wake is made-up of two longitudinal counter-rotating vortices. Ahmed (1981) confirmed the presence of these structures by performing wind tunnel tests on vehicle geometries with a notchback, estate and fastback rear-end shape, while Ahmed et al. (1984) did so by introducing and subsequently using the strongly simplified Ahmed body reference model with varying base slants. The added value of performing wind tunnel tests on the generic Ahmed body was that the results confirmed that the steady-state near wake separation bubble is the product of a merging process between multiple horseshoe vortices stacked on top of each other (Ahmed et al. 1984).

The experimental findings on the Ahmed body were largely corroborated by the numerical study of Han (1989), possibly some of the earliest numerical work on bluff-body aerodynamics. Specifically, Han (1989) performed finite volume method (FVM) based Reynolds-averaged Navier–Stokes (RANS) simulations of the Ahmed body with

rear slant, where the turbulence closure model selected was the  $k - \epsilon$  turbulence model. Through these simulations, access to the full 3D flow field surrounding the bluff-body was provided for the first time, thereby opening the door to a more comprehensive analysis of the interactions between the various structures dominating the bluff-body wake's steady-state behavior. However, Bearman (1997) began questioning whether a time-averaged simulation approach, like RANS, is truly capable of accurately capturing the steady-state behavior of the wake that results from complex transient motions of multiple vortices interacting with each other. There was after all some discrepancy between the simulated drag coefficient and base pressure results from Han (1989) and those found experimentally by Ahmed et al. (1984). As such Krajnović and Davidson (2003) moved on to perform FVM based inherently transient large eddy simulations (LES) with the Smagorinsky subgrid scale (SGS) turbulence model of the wake behind a generic bus shaped bluff-body geometry. One aim being to time-average the results, thereby obtaining information on the steady-state flow structures directly from the transient flow phenomena. Krajnović and Davidson (2003)'s simulations went on to confirm the RANS findings from Han (1989): the shear layers that encompass the steady-state toroidal structure of the near wake interact with the separation bubble to produce the counter-rotating longitudinal vortices further downstream.

Many investigations of bluff-body wakes now focus on the wake's time-dependent behavior: important road vehicle design considerations, such as tank slosh, gearbox lubrication, greenhouse wind noise, brake thermal performance, underhood cooling, soiling and tyre hydroplaning tendencies, all rely on a thorough understanding of the transient flow phenomena surrounding and within a road vehicle (Krajnović and Davidson 2003; Gaylard et al. 2013; Kotapati et al. 2009; Charpentier et al. 2016; Ambrose et al. 2018). Grandemange et al. (2012) observed for the first time experimentally that the initially spanwise symmetric laminar 3D wake aft of the squareback Ahmed body bifurcates to a state of permanent broken reflectional symmetry in the spanwise direction once a critical  $Re_H$  of 340 is attained. Wake unsteadiness, initiated through further incremental increase in  $Re_H$ , triggers asymmetries in the wake's topology that eventually push the wake into an off-axis spanwise configuration. The chosen off-axis spanwise position of the wake is maintained while in the laminar regime; there is no meandering of the wake between opposing off-axis positions (Grandemange et al. 2012). Evstafyeva et al. (2017) confirmed this unsteady behavior of the squareback Ahmed body's laminar wake by performing LES with and without the wall-adapting local eddy-viscosity (WALE) turbulence model, thereby providing full access to the flow field surrounding the Ahmed body. Their simulations suggest that, upon raising the  $Re_H$ , a point is eventually reached where sufficient underbody flow is present to allow the closer top and bottom parallel shear layer interaction to dominate over its spanwise counterpart. This in turn permits the main vortex structures in the wake to be vertically, as opposed to horizontally, aligned (Evstafyeva et al. 2017).

Upon raising the  $Re_H$  to a turbulent value, it has been observed that the wake asymmetry due to the laminar bifurcation remains. This was conclusively assessed by Rigas et al. (2014) who experimentally for an axisymmetric blunt bluff-body at  $Re_H \sim 2 \times 10^5$  noted that the large-scale coherent structures found within the 3D turbulent wake keep statistically the structure seen in the laminar symmetry breaking instabilities. However, unlike with the laminar wake, the turbulent wake aft of the axisymmetric blunt bluff-body is multi-stable and presents an infinite number of symmetry breaking modes. For a rectilinear 3D blunt bluff-body, like the squareback Ahmed body, this translates to a wake feature known as bimodality where the wake transitions at random time intervals between two opposing off-axis positions.

The unsteady side force caused by wake bimodality is believed to be responsible for up to 7% of bluff-body drag (Grandemange et al. 2014). As such, many recent studies, both experimental and numerical, have been conducted to obtain a better understanding of wake bimodality. The seminal work of Grandemange et al. (2013b) is likely the earliest work on wake bimodality. It highlights through experimental data that the instantaneous flow field aft of the squareback Ahmed body presents two modes over two distinct characteristic time-scales, respectively: at short time-scales of  $T_s \sim 5H/|U_\infty|$ , where  $|U_\infty|$  is the magnitude of the free-stream flow velocity, the wake field is dominated by the coherent flow oscillations associated with the vortex shedding mode, while at long time-scales of up to  $T_l \sim 1000H/|U_\infty|$ , the wake exhibits the large-scale spanwise shifts of its toroidal structure as part of the bimodal mode. In the hope of obtaining a better understanding of the bimodal wake's topology, various experimental studies employed 2D particle image velocimetry (PIV) planes: Evrard et al. (2016) conjecture that the asymmetric wake is composed of a single horseshoe vortex system, while both Perry et al. (2016) and Pavia et al. (2018) suggest that the instantaneously asymmetric wake is made up of a system comprising multiple horseshoe vortices. However, transient numerical simulations, spanning finite volume, lattice Boltzmann and spectral methods, of various squareback bluff-bodies, including the ground transportation system (GTS) model, have conclusively shown that the instantaneously asymmetric wake is made up of its time-averaged toroidal structure and is merely tilted to a given side (Lucas et al. 2017; Pasquetti and Peres 2015; Rao et al. 2018a, b; Dalla Longa et al. 2019).

Additionally, due to the bimodal wake's drag enhancing nature, numerous attempts, both passive and active, to attenuate the asymmetric wake and its bimodal dynamics have been made. Evrard et al. (2016) and Lucas et al. (2017) performed passive flow control by appending a cavity to the squareback Ahmed body, thereby symmetrizing the wake and reducing the drag by 9% and 9.5%, respectively. Meanwhile, Li et al. (2016) and Brackston et al. (2016) employed active flow control consisting of slot jets coupled to a physics based controller and oscillating flaps driven by a 2D non-linear Langevin equation model of the system (Rigas et al. 2015), respectively, in turn attenuating the reflectional symmetry breaking modes and raising the blunt bluff-body's base pressure. A further study by Grandemange et al. (2014) was also able to raise the Ahmed body's base pressure by symmetrizing the otherwise asymmetric wake and elongating the recirculation bubble length. This time, a vertical control cylinder was used to apply a steady symmetric force to the wake.

In light of the importance of attenuating bimodality for improving bluff-body drag characteristics, several studies have focused on understanding bimodality's source. The FVM based WALE LES results from Dalla Longa et al. (2019) suggest that a hairpin vortex shed from the separating shear layers at the bluff-body's trailing edge helps trigger a bimodal switch. This finding appears to be reconfirmed by the corresponding FVM based improved delayed detached eddy simulation (IDDES) results from Fan et al. (2020). Podvin et al. (2021), however, suggest with their proper orthogonal decomposition (POD) analysed direct numerical simulation (DNS) results that an increase in vortex shedding activity is responsible for the initiation of a bimodal switching event. Finally, by performing both wall-resolved (WRLES) and wall-modelled (WMLES) LES, Hesse and Morgans (2021) suggest that powerful hairpin vortices shed from the front recirculation bubbles located just aft of the Ahmed body nose are responsible for triggering bimodal wake switching events.

Simplified bluff body shapes, like the Ahmed body, are useful for relating observed flow phenomena to their origin. They namely act as a geometrical filter on the flow field and, in doing so, provide a better signal-to-noise ratio. This leads to an improved understanding

of basic bluff-body flow structures (Gaylard et al. 2017). In fact, with the growth of the battery electric vehicle market, where vehicles have good grille and underbody shutters for closing the air inlets, simplified bluff-body geometries are becoming more relevant and representative of on-road vehicle shapes (Linuma et al. 2018). Nonetheless, their abstraction is still a departure from most on-road vehicles. Therefore, the study of interference effects between fundamental bluff-body flow structures and more complex shapes associated with a vehicle, such as the tires, the A-pillars, the air inlets, and more, must be done (Heft et al. 2012).

For this reason, two experimental studies focusing on the bimodal wake characteristics of industry relevant road vehicle geometries have been performed (Bonnaivon et al. 2017, 2019). Bonnaivon et al. (2017) varied the yaw angle of the flow incident on the Renault Kangoo, thereby identifying wake bimodality in the vertical direction, which is reminiscent of wake bimodality in the spanwise direction aft of the Ahmed body, at a yaw angle of approximately  $4^\circ$ . Surprisingly, the drag value remained independent of the yaw angle and, therefore, the chosen state of the bimodal wake. The same cannot be said of the lift value, which, depending on the current wake state, could rise by as much as 27%. This shows that the careful selection of the bimodal wake's state is crucial to vehicle ride stability. Bonnaivon et al. (2019) went on to perform a similar study on the Peugeot 5008, Peugeot Partner and Citroën Berlingo. In this case, not only was the incident flow's yaw angle varied, but also the ground clearance, pitch and air intake configuration (open or closed) was modified as well. As in the previous study by Bonnaivon et al. (2017), here too it was found that the lift value depends heavily on the bimodal wake's current orientation in the vertical direction. However, it was also found that the drag value is lower for a wake tilted away from the vehicle's top trailing edge, illustrating that the selection of a desired bimodal wake state can improve the drag characteristics of the vehicle.

Additionally, there have also been numerical investigations featuring more on-road representative vehicle shapes. Ashton et al. (2016) simulated the flow past the benchmarked DrivAer model with the goal of identifying the benefits and drawbacks associated with using hybrid RANS-LES methods, in this case detached eddy simulation (DES), over industry standard RANS simulations for automotive applications. A similar study was performed by Aljure et al. (2018) who assessed the benefits of using CPUhr cheaper WMLES, where a RANS based wall-model is active in the near-wall flow region thereby avoiding the need to fully resolve the turbulent boundary layer, compared to WRLES for simulating the flow past the fastback variant of the DrivAer model.

While these numerical investigations proved vital to obtaining access to the full transient flow field past an on-road representative vehicle shape, the studies did not focus on the wake asymmetries nor bimodal wake characteristics of industry relevant road vehicle geometries. The following study using WRLES at a  $Re_H$  of 100,000 for a 15% scale model hopes to overcome this deficiency of past numerical studies by, as a preliminary study of bimodal wake behavior, assessing the wake asymmetries that characterize the wake behind the Nissan NDP (Fig. 1). The NDP, which stands for New Driving Position, is an electric concept vehicle developed by Nissan as part of a loading bay optimization study featuring their production vehicle, the Nissan NV200, and was used to determine the benefits of doing wind tunnel tests under more unsteady and non-zero yaw conditions (Kremheller et al. 2015, 2016). Both a “squareback” (Fig. 1b) and passively controlled cavity variant (Fig. 1a) of the Nissan NDP are looked at closely to assess the wake asymmetries present and their implications for bimodal wake behavior, as well as to understand the effect of the cavity on various integral flow quantities such as the drag coefficient,  $C_D$ . A second objective of this paper is to compare the unsteady wake dynamics present for the Nissan NDP

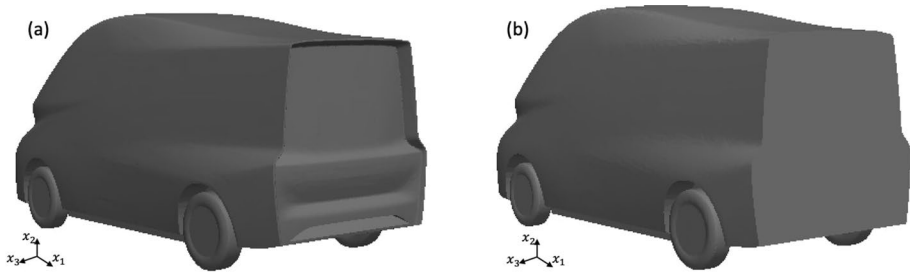


**Fig. 1** Nissan NDP rear topology: **a** with cavity and **b** “squareback” variant

when doing stationary ground simulations with those exhibited when performing moving ground simulations.

The remainder of this paper is structured as follows. Section 2 describes the numerical environment. This includes a detailed description of the computational set-up as well as an overview of the POD post-processing technique, which is used heavily throughout the results section of this paper. Meanwhile, Sect. 3 reviews the findings of the study, while Sect. 4 concludes the study (Hesse 2021).

## 2 Numerical Environment

### 2.1 Geometry and Flow Domain

The geometry under investigation is the 15% scale model of the Nissan NDP, an electric concept vehicle developed by Nissan (Fig. 1). To allow interested parties to reproduce the subsequent work, the surface mesh representation, in the form of an STL file, for each variant is appended to this work as supplementary material.

A 15% scale model is chosen in order to keep the  $Re_H$  at an order of magnitude, specifically  $\mathcal{O}(10^5)$ , that is still reasonable for WRLES in terms of CPUhrs (Reynolds 1990; Piomelli and Balaras 2002; Piomelli 2008). Aljure et al. (2018) has namely shown that a WRLES simulation for a full-scale DrivAer vehicle with the more realistic  $Re_H$  of  $\mathcal{O}(10^6)$  takes 11 days and  $2.78 \times 10^5$  CPUhrs to run, and only simulates a non-dimensional time span,  $t^* = t|U_\infty|/H$ , of approximately 8 units. Therefore, although it is computationally feasible to run full-scale vehicle simulations, where  $Re_H$  is of  $\mathcal{O}(10^6)$ , using cheaper CFD methods, such as RANS and hybrid RANS-LES, it is not amenable to run this  $Re_H$  value for the current WRLES case (John et al. 2018; Aljure et al. 2018; Ashton et al. 2016). This is particularly true considering that the long time-scale ( $t^* \sim 1000$ ) wake bimodality phenomenon, which has been shown to already occur at  $Re_H$  of  $\mathcal{O}(10^4)$ , forms part of the current investigation on rear wake asymmetries (Hesse and Morgans 2021). Despite simulating a  $Re_H = 100,000$  flow field, the most pertinent bluff-body flow structures, such as A-pillar vortex, ceiling separation vortex and trailing edge vortices, are nonetheless resolved as illustrated in Sects. 3.1–3.2. The  $Re_H = 100,000$  NDP simulations are, thus, a good compromise between simulation cost and flow structure resolution.

Furthermore, the chosen 15% scale model size corresponds to the following vehicle dimensions: length of  $L = 0.657$  m, height of  $H = 0.309$  m and width of  $W = 0.257$  m. Meanwhile, the ground clearance is measured as  $G = 0.0251$  m. Based on the work of



Grandemange et al. (2013a), who investigated the presence of wake bimodality for squareback bluff-bodies of varying aspect ratio and ground clearance, there is the potential for both spanwise (i.e. in the  $x_3$ -direction) and vertical (i.e. in the  $x_2$ -direction) bimodal switches to occur. However, bimodal switches are only expected to happen in one direction per simulation run, as elucidated by Dalla Longa et al. (2019). Final assessment of the potential for bimodality to occur is done by looking at the detected wake asymmetries for both the “squareback” and cavity variants. Quotations are placed around the term squareback, as Fig. 1b shows that the vehicle trailing edge is not truly blunt. Additionally, tire spoke details are disregarded in this work and are replaced by a simple flat hub-cap in order to simplify the meshing process (see Sect. 2.5). For this same reason, the Nissan logo has been removed.

The computational domain size is chosen to be in line with best-practice guidelines specified by ERCOFTAC for bluff-body flows. As such, the computational domain,  $\Omega$ , is specified to be of the following size:  $\Omega = (L_{inlet}, L_{x_1}, L_{x_2}, L_{x_3}) = (2L, 8L, 2L, 2L)$  (Manceau and Bonnet 2002).

## 2.2 Solver Details

The computational fluid dynamics (CFD) tool chosen for this study is the open-source dimensional OpenFOAM solver. It solves the incompressible Navier–Stokes equations using the FVM. The various simulations carried out in this investigation were performed in a two-part process. This was done to accelerate the attainment of solution convergence and, thereby, save on numerical resources, while also ensuring solution stability. More specifically, the set-ups were first allowed to develop from a uniform initial flow state (see Sect. 2.3) to a steady-state using simpleFOAM combined with stable first-order accurate spatial schemes, as well as the stable single equation Spalart–Allmaras RANS turbulence model. SimpleFOAM is a solver used for incompressible turbulent flow problems and employs the time independent semi-implicit method for pressure linked equations (SIMPLE) algorithm to solve for the coupled velocity and pressure fields (Patankar and Spalding 1972; Spalart and Allmaras 1992). Once a steady-state flow field was reached, the pimpleFOAM solver was switched “on”. It propagates the solution forward in time by using a large time-step transient solver for turbulent incompressible flows. To be precise, pimpleFOAM employs the pressure implicit with splitting operators (PISO)—SIMPLE algorithm for evaluating the coupled velocity and pressure fields (Barton 1998). As accuracy is now paramount, second-order accurate temporal and spatial schemes were adopted for this part of the simulation workflow. To ensure that the solution field stays total variation diminishing (TVD), meaning there is no undershoot and overshoot created in the flow field, the Courant–Friedrichs–Lewy (CFL) number was maintained at an  $\mathcal{O}(1)$  while limiters were adopted for the solvers (Versteeg and Malalasekera 2007). The turbulence modelling approach chosen for the second portion of the simulation workflow is LES. More specifically, the WALE model developed by Nicoud and Ducros (1999) was chosen for its favourable characteristics over the classical Smagorinsky (1963) SGS model. WALE is, namely, able to replicate the turbulent eddy-viscosity’s cubic wall-asymptotic behavior while at the same time accounting for both the rotation and strain rate of the smallest resolved turbulent eddies, thereby better modelling the transfer of energy from the resolved scales to the sub-grid scales.

## 2.3 Boundary and Initial Conditions

To simulate a bluff-body flow at a reasonable  $Re_H$  of 100,000 for WRLES, where the fluid is modelled as air at  $20^\circ$  with a kinematic viscosity of  $1.511 \times 10^{-5} \text{m}^2 \text{s}^{-1}$ , at the domain inlet a uniform flow velocity of  $U_\infty = (4.893, 0, 0) \text{m s}^{-1}$  was specified. It is important to note that turbulence was permitted to develop naturally. There was no artificial turbulence forcing specified at the domain inlet. This, coupled to the fact that the flow field was initialised with a RANS simulation, meant that fully developed turbulent flow was achieved after about  $t^* = 6.3$  non-dimensional time units. At the domain boundaries located far-away from the Nissan NDP, that is at the domain sides and the top boundary, a free-slip condition was stipulated. Meanwhile, a pressure advection condition was applied to the domain outlet boundary to ensure pressure waves are not reflected back into the simulation domain. The Nissan NDP's walls were accounted for through the explicit enforcement of the no-slip condition. More specifically, the developing boundary layer was not modelled, but resolved by keeping the mean wall "y-plus",  $x_{w2}^+$ , at an order of magnitude of  $\mathcal{O}(1)$  (see Sect. 2.5). As both stationary ground and moving ground simulations were performed, the ground boundary condition was either a no-slip condition or set equal to the free-stream flow velocity of  $U_\infty = (4.893, 0, 0) \text{m s}^{-1}$ . Ideally, the rotational (and even deformation) effects of the wheels should also have been taken into account when doing the moving ground simulations through the application of a moving reference frame (MRF) or a sliding mesh (Alajbegovic et al. 2017). However, as the focus of this study is the rear wake of the Nissan NDP and its possible long time-scale bimodal characteristics, simplified tire modelling was kept as was done for the tires' geometry (see Sect. 2.1), thereby saving on simulation complexity and cost. Finally, the initial conditions of the simulations, that is the input to the RANS simulations, were a velocity field set to the free-stream flow velocity of  $U_\infty = (4.893, 0, 0) \text{m s}^{-1}$  and a pressure field set to a gauge pressure of  $P = 0 \text{Pa}$ .

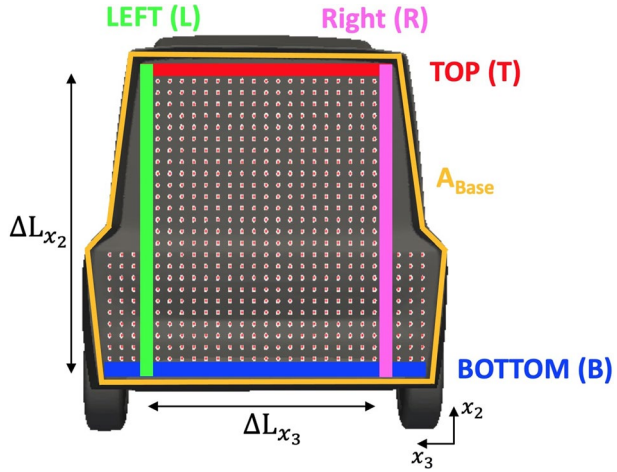
## 2.4 Definition of Key Variables

Several important variables that are used throughout this investigation need to be defined. These variables build on the flow velocity,  $U$ , and pressure,  $P$ . Specifically, the drag coefficient,  $C_D$ , lift coefficient,  $C_L$ , pressure coefficient,  $C_p$ , and base pressure coefficient,  $C_{pB}$ , need to be stipulated. The base pressure coefficient,  $C_{pB}$ , is derived from the pressure coefficient,  $C_p$ , of  $n$  equal to 633 probes distributed over the rear base area of the vehicle,  $A_{Base}$  (see Fig. 2). Equations (1) to (3) define these integral flow variables, where  $F_D$  is the integrated drag force acting on the vehicle,  $F_L$  is the integrated lift force exerted on the vehicle,  $P_\infty$  is the free-stream pressure,  $\rho_\infty$  is the free-stream fluid density,  $A_{x_2x_3}$  is the vehicle area projected onto the  $x_2x_3$ -plane, and  $A_{x_1x_3}$  is the vehicle area projected onto the  $x_1x_3$ -plane. Furthermore, unless otherwise stated, throughout this paper the use of an over-bar denotes time-averaging that starts at approximately  $t^* = 6.3$  non-dimensional flow units, which is when the flow field is considered fully developed, and is propagated to about  $t^* = 55$  non-dimensional flow units. This ensures that about 10 cycles of the vortex shedding mode, which is associated with a non-dimensional time-scale of about  $t^* = 5$ , are captured for statistical convergence (Grande-mange et al. 2013b).

$$C_D = \frac{F_D}{\frac{1}{2} \rho_\infty |U_\infty|^2 A_{x_2x_3}} \quad (1)$$



**Fig. 2** Rear base pressure probe array with left (L), right (R), top (T) and bottom (B) linear arrays



$$C_L = \frac{F_L}{\frac{1}{2} \rho_\infty |U_\infty|^2 A_{x_1 x_3}} \tag{2}$$

$$C_P = \frac{P - P_\infty}{\frac{1}{2} \rho_\infty |U_\infty|^2} \rightarrow C_{PB} = \frac{\sum_{i=1}^{n=633} C_{P_i} dA}{A_{Base}} \tag{3}$$

As this investigation attempts to identify the presence or absence of bimodal wake behavior for the Nissan NDP, two derivative quantities need to be defined as well. These are the spanwise,  $\partial C_P / \partial x_3$ , (Eq. 4) and vertical,  $\partial C_P / \partial x_2$ , (Eq. 5) base pressure gradients, respectively. Subsequent definitions are made with reference to Fig. 2, which depicts the positioning of the pressure probes on the NDP’s rear base for its cavity variant; the probe positions apply equally to the “squareback” version of the NDP. Figure 2 highlights four linear probe arrays: a left (L) and right (R) vertical array separated by a spanwise distance of  $\Delta L_{x_3}$ , as well as a top (T) and bottom (B) spanwise array separated by a vertical distance of  $\Delta L_{x_2}$ . The spanwise gradient is defined as the difference between the spatial mean of the left (L) array and the spatial mean of the right (R) array divided by the non-dimensional separation distance. A similar definition, except in the vertical direction for top (T) and bottom (B) probe arrays, applies for the vertical base pressure gradient.

$$\frac{\partial C_P}{\partial x_3} = H \frac{\overline{C_{P_L}} - \overline{C_{P_R}}}{\Delta L_{x_3}} \tag{4}$$

$$\frac{\partial C_P}{\partial x_2} = H \frac{\overline{C_{P_T}} - \overline{C_{P_B}}}{\Delta L_{x_2}} \tag{5}$$

This study also looks at vortex structures, which requires the definition of a further two quantities: vorticity,  $\omega$ , and Q-criterion,  $Q$ . Vorticity is defined as the curl of the velocity field (Eq. 6), highlighting that vortex structures are regions of high rotation rate.

Meanwhile, the  $Q$ -criterion (Eq. 7) is defined as the Laplacian of pressure,  $P$ , which can be reformulated to be the difference between the double contraction of the spin tensor,  $\mathbf{W}$ , and strain rate tensor,  $\mathbf{S}$ , again illustrating that vortex structures are regions of high rotation rate with a positive  $Q$ -value. At this stage, it is also useful to introduce the non-dimensional form of the  $Q$ -criterion (Eq. 8), which is derived with the help of the free-stream velocity magnitude,  $|U_\infty|$ , and body base height,  $H$ .

$$\boldsymbol{\omega} = \nabla \times \mathbf{U} \quad (6)$$

$$Q = \nabla^2 P = \mathbf{W} \cdot \cdot \mathbf{W} - \mathbf{S} \cdot \cdot \mathbf{S} \quad (7)$$

$$Q \rightarrow Q^* = \frac{QH^2}{|U_\infty|^2} \quad (8)$$

## 2.5 Mesh Refinement Study

Prior to any fluid domain mesh creation, the Nissan NDP geometry needed to be wrapped using a surface wrapper feature available in the commercial CFD solver Star-CCM+. The reason for this geometry work is that the CAD model provided by Nissan had too many self-intersecting and overlapping facets, preventing the direct creation of a tessellated surface mesh. Once the surface mesh was created using the surface wrapper, the fluid domain mesh was generated using Star-CCM+'s built-in meshing capabilities. These meshes were subsequently converted to OpenFOAM format using a mesh conversion utility called `ccm26ToFoam`.

The majority of the fluid domain was meshed using trimmer cells. These are hexahedral cells that on approach to geometry boundaries are trimmed to conform to the simulated object's shape (Fig. 3b–c). In doing so, polyhedral cells are created close to the vehicle geometry. Trimmer cells were chosen for the fluid domain, as they are computationally efficient mesh elements for flow set-ups with a primary flow direction, as is the case for external aerodynamic simulations. At geometry walls, prism layer cells were positioned, as these orthogonal prismatic elements are good for capturing the steep gradient of turbulent boundary layer velocity profiles without exorbitantly increasing the mesh count in the far-field of the domain (Fig. 3a). Overall, unstructured, rather than structured, meshes were produced and used in this investigation of the Nissan NDP's rear wake topology.

Identification of the baseline mesh to use throughout this investigation was done by performing a mesh refinement study. The set-up used for the study was the moving ground simulation of the Nissan NDP with cavity appendage. This is because stipulating a moving ground means no turbulent boundary layers with their steep velocity gradients develop at the ground boundary, thereby avoiding the need to position cell count increasing prism layer cells at the ground of the computational domain. Other aerodynamic virtual wind tunnel studies such as the papers by Ljungskog et al. (2020) and Aljure et al. (2018) adopt an identical meshing strategy for moving ground simulations and this saves CPUhrs. Furthermore, the wake refinement region, as depicted in Fig. 3, is defined in Star-CCM+ as a projection, approximately 1.5 vehicle lengths backwards, of the NDP vehicle's shape. It, hence, takes on the contour of the NDP's shape. Meanwhile, a scaling relationship in the form of Eq. (9) was used to obtain an estimate of the necessary, but not always sufficiently small, wake cell size needed to resolve the eddies down to the Taylor microscale.

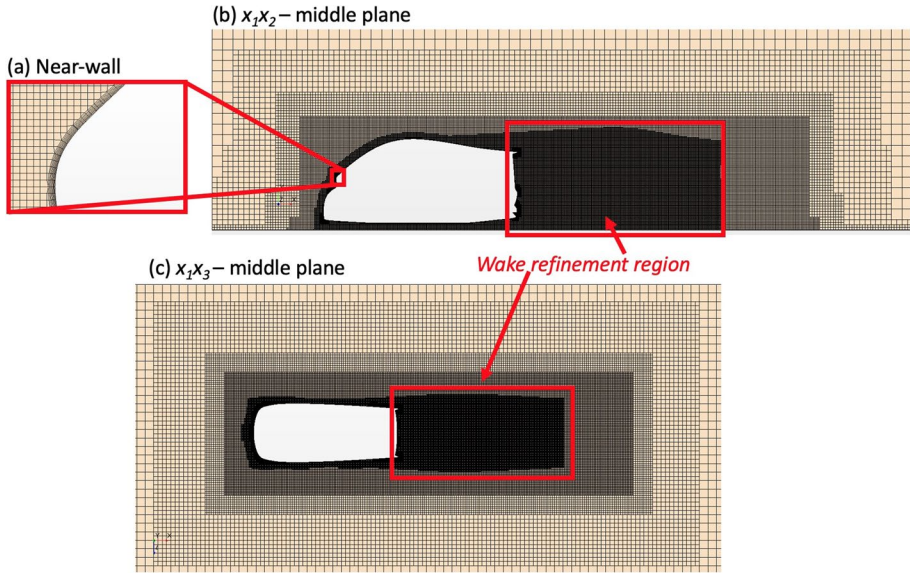


**Fig. 3** Sample fluid domain mesh with **a** prism layer cells near the Nissan NDP wall, and trimmer cells in the majority of the flow domain visualized on the **b**  $x_1x_2$ —middle plane and **c** the  $x_1x_3$ —middle plane

The Taylor microscale is the reference eddy size below which eddy scale isotropy can be reasonably assumed to hold and below which eddy dynamics is heavily influenced by viscosity. Equation (9), therefore, provides a ballpark estimate for the eddy size below which the use of an eddy-viscosity based LES turbulence model can be used to account for unresolved eddy physics. The relationship is obtained by assuming a homogeneous and steady shear flow where the viscous dissipation of turbulent energy is equivalent to its production.  $l$  is the integral (large) eddy length-scale, while  $A$  is a yet to be determined constant of order one (Tennekes et al. 1972). As has been done in other bluff-body simulation work,  $A$  is set equal to 0.5, while  $l$  is the bluff-body height,  $H$  (Guilmineau et al. 2018; Howard and Pourquie 2002).

$$\lambda_T \sim 15^{\frac{1}{2}} A^{-\frac{1}{2}} Re_l^{-\frac{1}{2}} l \rightarrow \lambda_T \sim 5.5 Re_H^{-\frac{1}{2}} H \tag{9}$$

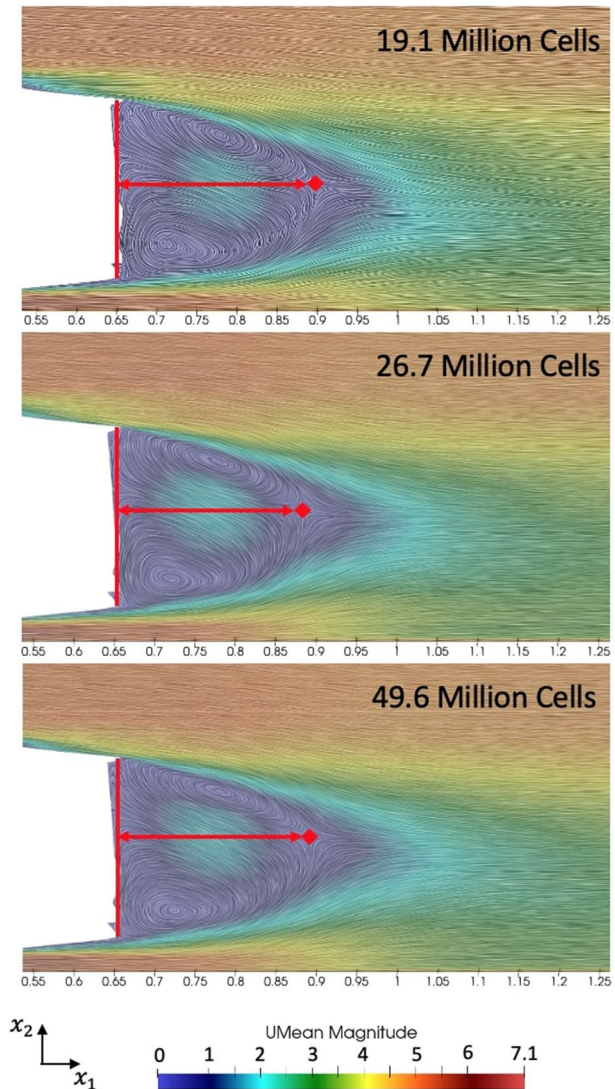
Mesh refinement study results are presented in Table 1. A total of three mesh constructions were simulated. Each set-up had a wake cell size that is a factor two smaller than its coarser predecessor. At the end, the second mesh set-up was chosen. It has approximately 26.7

**Table 1** Mesh refinement study based on Nissan NDP with cavity appendage and moving ground—mean flow quantities

Mesh size	$\Delta L_{wake}$	CPUhrs ( $t^* = 1$ )	$\overline{C_D}$	$\overline{C_L}$	$\overline{C_{PB}}$	$\overline{L_B}$
19.1 million	$0.832\lambda_T$	1366	0.263	-0.0828	-0.188	0.797 H
26.7 million	$0.417\lambda_T$	1834	0.265	-0.0888	-0.190	0.754 H
49.6 million	$0.205\lambda_T$	9715	0.271	-0.0918	-0.192	0.780 H

million cells and is of intermediate wake resolution. This means using the mesh is not too expensive in terms of CPUhrs. In fact, as Table 1 shows, the CPUhrs for simulating up to  $t^* = 1$  only increase by 34% between the coarsest mesh and the mesh of intermediate wake refinement, while moving to the finest mesh requires a CPUhr increase of 611%. At the same time, the mesh of intermediate wake resolution exhibits a reasonably well stabilized average base pressure,  $\overline{C_{PB}}$ . There is some variation in recirculation bubble length,  $\overline{L_B}$ . However, as Fig. 4 demonstrates, this variation is almost imperceptible and can be attributed to the recirculation bubble closing (i.e. having its saddle point) further upstream for the chosen baseline mesh of 26.7 million cells. There is some additional discrepancy for  $\overline{C_D}$  and  $\overline{C_L}$  when comparing the second set-up with the finer third variant. However, when

**Fig. 4** Recirculation bubble visualization for the three mesh set-ups using the mean velocity field for the surface image and line integral convolution (LIC)



considering the large time-scales that characterize wake bimodality, namely  $t^* \sim 10^3$ , it was deemed intractable from a computational viewpoint to go with the finer mesh set-up. This will be touched upon further in Sect. 3.1. The struggle to achieve mesh convergence for  $\overline{C_D}$  and  $\overline{C_L}$  illustrates that acquiring converged surface measurements in CFD is not simple. The reason for this difficulty is that these measurements are taken where the surface mesh intersects the volume mesh and is, therefore, where complex interpolation operations take place. Similar issues in obtaining converged force coefficients were encountered in the study by Fan et al. (2020). In their study, there is a 2.6% variation in  $\overline{C_D}$  between their coarsest and finest mesh, while in the present study on the NDP the variation lies at 3.0%.

A further indicator that the mesh of intermediate resolution is appropriate is an analysis of resolved versus modelled turbulence. This is done by looking at iso-contour plots of the instantaneous turbulent eddy viscosity ratio,  $\nu_t/\nu$ , where higher values are enclosed (Fig. 5). The iso-contour values chosen are  $\nu_t/\nu = 5$  (Fig. 5a) and  $\nu_t/\nu = 10$  (Fig. 5b). Looking at these plots, it is important to note that the large contours in the vehicle’s far-field wake region should be disregarded. They are attributed to the WALE eddy viscosity’s length-scale dependency on the local mesh size and, therefore, the associated large cell sizes in the far-field wake region. This has been pointed out in the LES work of the reference Ahmed body by Howard and Pourquie (2002). Meanwhile, in the near-field wake region where, to varying amounts, physical strain effects are modelled by the WALE LES turbulence model, one can see that the level of modelled turbulence plateaus between the 26.7 million cell mesh and the 49.6 million cell mesh. Both meshes have similar instantaneous iso-contour plots of  $\nu_t/\nu$  in the near-field wake region. It is, therefore, deemed appropriate to choose the 26.7 million cell mesh as the baseline mesh.

At this stage, one may wonder whether using a coarser mesh might affect the possibility of resolving wake bimodality with the Nissan NDP. As Sects. 3.1 and 3.2, where the flow

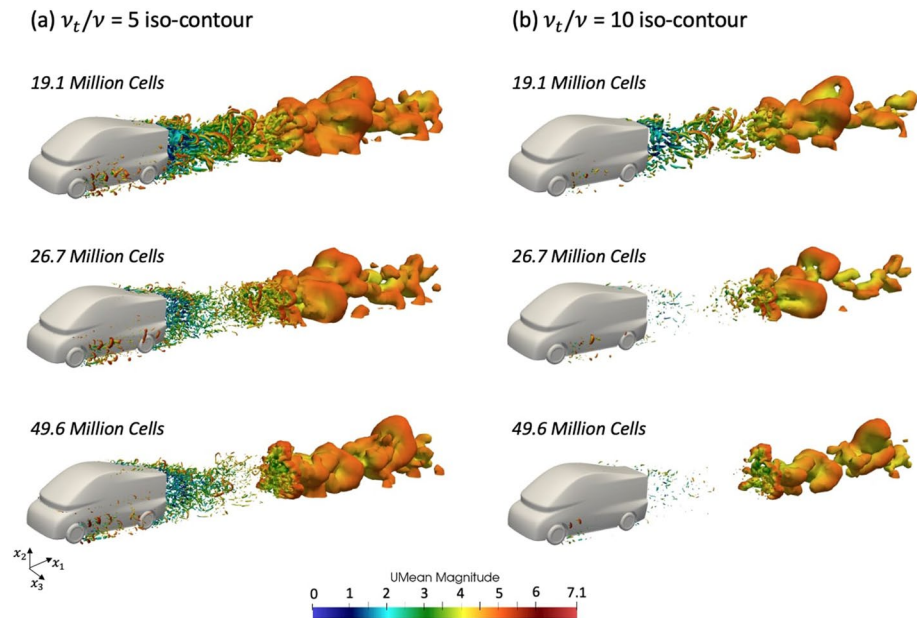


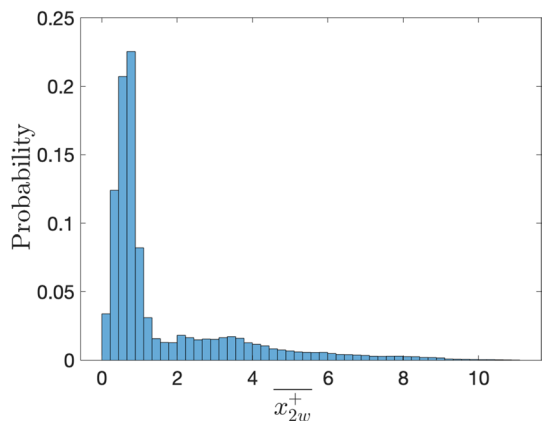
**Fig. 5** Measure of resolved turbulence versus modelled turbulence for the three mesh set-ups through visualization of iso-contour plots of **a**  $\nu_t/\nu = 5$  and **b**  $\nu_t/\nu = 10$  colored by mean velocity magnitude



field around the Nissan NDP is analysed, illustrate, the relevant flow structures seem to be resolved with the grid of intermediate resolution. More specifically, the notable vertical wake asymmetry is resolved (Figs. 11 and 19), which implies that the wake balance in the vertical direction is accurately captured, while a large hairpin vortex shed from the vehicle's roof (Figs. 18, 19, 20, 21, 22, 23 and 24) is also resolved. Based on the work of Hesse and Morgans (2021), where it was determined that the large hairpin vortices shed from the front recirculation bubble with high TKE content are a likely source for triggering a bimodal wake switching event, the capturing of the above mentioned flow features should be sufficient for resolving bimodality, if it is present with the NDP. As a matter of fact, based on the above assertion, it would even be plausible to continue the wake flow analysis with the coarsest mesh consisting of 19.1 million cells. The reason being, it captures the pertinent flow structures as well. However, to make sure that enough wake flow unsteadiness is captured, one has ultimately decided to use the mesh of intermediate resolution. Ideally, comparison with experimental data should also be done. Unfortunately, no such data is currently available for the Nissan NDP simulated at  $Re_H$  of 100,000.

Having conclusively determined the wake and far-field mesh, the near-wall mesh is subsequently analyzed. Carrying out WRLES necessitates that the time-averaged wall “y-plus”,  $x_{w2}^+$ , be dominated by a value of one (Fan et al. 2020). Looking at Fig. 6, this is indeed true. By projecting the mean wall “y-plus” values onto the vehicle surface (Fig. 7), more insight is acquired as to where values of  $x_{w2}^+ > 1$  are located. These values of  $x_{w2}^+$  are positioned in the locality of the tires. As described in Sects. 2.1 and 2.3, accurate replication of flow dynamics around the tires, whose contact patch is treated by placing the tires on small pedestals, is not a priority in this study; the emphasis in this study is the large-scale flow separation at the NDP's trailing edge. Hence, the reason for the simplified tire geometry, and negligence of tire deformation and rotation. As such, additional errors introduced to the tire flow field by its under-resolution are deemed acceptable, especially if a computationally more efficient mesh is created. It is also necessary to look at the near-wall time-averaged streamwise,  $\Delta x_{w1}^+$ , and spanwise,  $\Delta x_{w3}^+$ , cell spacing, ensuring that they fulfill the requirements for WRLES as dictated by the work of Choi and Moin (2012). More specifically, Choi and Moin (2012) stipulate that  $\Delta x_{w1}^+$  should be at most between 50 and 130, while  $\Delta x_{w3}^+$  should lie at most between 15 and 30. In this work,  $\Delta x_{w1}^+$  and  $\Delta x_{w3}^+$  are equal to each other i.e. near-wall cells are isotropic in the streamwise and spanwise directions. The mean value of  $\Delta x_{w1}^+$  and  $\Delta x_{w3}^+$  lies at approximately 18.4, indicating that

**Fig. 6** Histogram plot of time-averaged wall “y-plus”,  $x_{w2}^+$ , for the Nissan NDP with moving ground





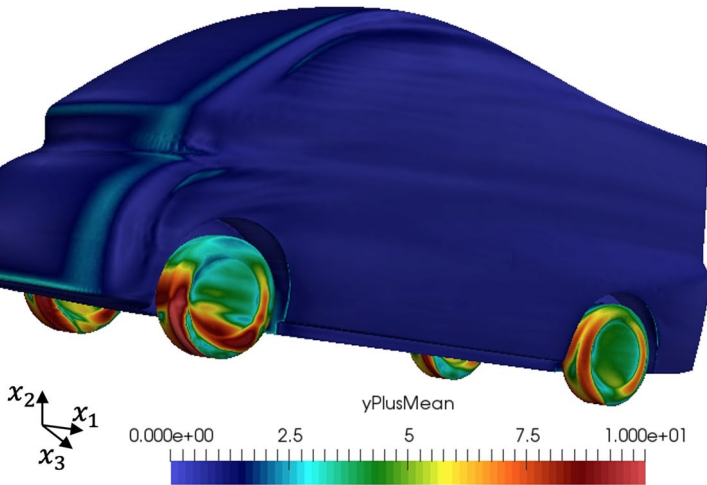


**Fig. 7** Time-averaged wall “y-plus” projected onto the Nissan NDP surface

the constructed near-wall mesh is slightly over-resolved in the streamwise direction, while being well within the WRLES mesh criteria for the spanwise direction.

Subsequently derived flow domain meshes, which include one for the “squareback” NDP with stationary ground and one for the cavity variant of the Nissan NDP with stationary ground, maintain identical trimmer cell and prism layer mesh constructions for away from and near to the NDP walls, respectively, as the above mentioned 26.7 million cell mesh for the moving ground simulation of the cavity variant. The stationary ground meshes do, however, also have prism layers constructed at the ground boundary in order to capture the velocity gradient of the stationary ground’s developing boundary layer.

## 2.6 POD Post-Processing

Due to the complexity of flow fields, which exhibit a very broad range of spatio- and temporal-scales, it is advantageous to be able to break the fluid problem down into physically important coherent flow structures, also known as modes. A low-dimensional problem consisting of the most pertinent modes can then be developed to subsequently construct more targeted and efficient flow control algorithms that, for example, reduce bluff-body drag. A large part of Sect. 3 relies on the use of such a model-order reduction technique to analyse the flow field. Specifically, the data-based proper orthogonal decomposition (POD) post-processing technique is heavily used (Taira et al. 2017).

POD, first introduced into the fluid dynamics community by Lumley (1967), extracts coherent flow structures by breaking down the provided data set into a minimum number of basis functions that together encompass the majority of the fluid flow energy. This means that POD captures and ranks modes based on energy content. The specific algorithm used in this study relies on three steps, as outlined below.

1. First, a time series of flow field snapshots is collected. From these snapshots, the considered variable’s mean is deducted. This means, only fluid flow fluctuations that are represented by the data vector  $\mathbf{y}$  are of significance (Taira et al. 2017).

$$\mathbf{y}(x_i, t) = \mathbf{q}(x_i, t) - \bar{\mathbf{q}}(x_i) \in \mathbb{R}^n, \quad t = t_1, t_2, \dots, t_m \quad (10)$$

2. Next, the  $m$  flow field snapshots are collected into a matrix,  $\mathbf{Y}$ , of the form illustrated below (Taira et al. 2017).

$$\mathbf{Y} = [\mathbf{y}(t_1), \mathbf{y}(t_2), \dots, \mathbf{y}(t_m)] \in \mathbb{R}^{n \times m} \quad (11)$$

3. Finally, the singular value decomposition (SVD) of the matrix  $\mathbf{Y}$  is computed. The matrix deconstruction is provided below for  $m < n$ :  $\Phi \in \mathbb{R}^{n \times n}$  is the left singular matrix,  $\Psi \in \mathbb{R}^{m \times m}$  is the right singular matrix and  $\Lambda \in \mathbb{R}^{n \times m}$  is a diagonal matrix that contains the corresponding singular values  $(\Lambda_1, \Lambda_2, \dots)$  (Taira et al. 2017).

$$\mathbf{Y} = \Phi \Lambda \Psi^T \quad (12)$$

The POD modes' spatial structure is dictated by the left singular matrix,  $\Phi$ , while the energy content of the different POD modes is provided by the singular values through the relationship  $\lambda_j = \Lambda_j^2$  (Taira et al. 2017).

In the present work,  $m$ , which is dictated by the length of the simulation and time-step size, was approximately 750, while  $n$ , which is set by the number of finite volume cells associated with the measurement plane for POD, was of  $\mathcal{O}(10^5)$ .

### 3 Results

This section involves two comparisons. First, the “squareback” variant of the NDP is compared to its cavity variant, during which an assessment of wake asymmetries is performed and the potential for wake bimodality to occur is also analyzed. After that, a stationary ground simulation is compared to its moving ground counterpart to assess the pros and cons of using a moving ground for vehicle development.

#### 3.1 “Squareback” Versus Cavity Variant

The two simulations analysed in this section use a stationary ground. Before moving on to the analysis, it is important to note that the results discussed here on the presence or absence of wake bimodality in the spanwise and/or vertical direction for either variant are not conclusive. The reason for this is that only a small portion of the non-dimensional time window,  $t^*$ , in which bimodality can be expected to occur in, namely  $t^* = 1000$ , was simulated (Grandemange et al. 2013b). Despite using up about  $4.0 \times 10^5$  CPUhrs, a non-dimensional simulation time span of merely  $t^* \sim 60$  was accomplished (Figs. 8 and 9). This highlights that, while simulating the vortex shedding mode, which has  $t^* \sim 5$ , is very feasible, it is extremely difficult to simulate wake bimodality, particularly for  $Re_H$  approaching the order of magnitudes encountered on the road, namely  $\mathcal{O}(10^6)$ .

Figures 8 and 9 illustrate the vertical and spanwise base pressure gradient for the “squareback” and cavity variant of the NDP, respectively. One can immediately identify a very prominent wake asymmetry in the vertical direction for both setups (Figs. 8a and 9a). Causes for this asymmetry in the vertical direction are the presence of the ground, the vertical asymmetry of the vehicle's geometry, as well as a powerful hairpin vortex that detaches directly in the middle of the NDP's roof, between the rear and front axle—this flow structure is visually shown in Sect. 3.2 (Figs. 18, 19, 20, 21, 22, 23 and 24).

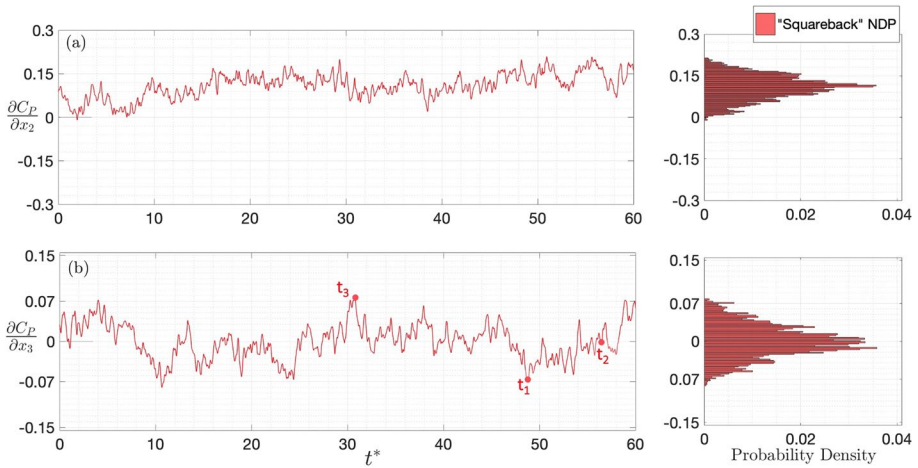


**Fig. 8** Base pressure gradient in the **a** vertical direction,  $\partial C_p/\partial x_2$ , and **b** spanwise direction,  $\partial C_p/\partial x_3$ , for the Nissan NDP without cavity appendage. Filled-in circles denote times at which instantaneous pressure snapshots are taken for Fig. 12

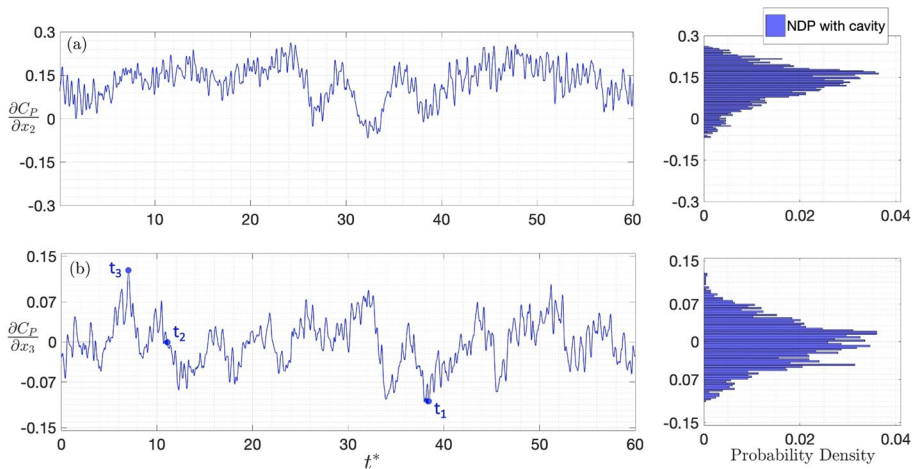


**Fig. 9** Base pressure gradient in the **a** vertical direction,  $\partial C_p/\partial x_2$ , and **b** spanwise direction,  $\partial C_p/\partial x_3$ , for the Nissan NDP with cavity appendage. Filled-in circles denote times at which instantaneous pressure snapshots are taken for Fig. 13

Figures 8a and 9a also illustrate that the cavity variant of the NDP allows the rear wake to explore a larger vertical base pressure gradient space compared to its “squareback” form. On the other hand, no distinct long-term rear wake asymmetry in the spanwise direction is detected when looking at the base pressure gradient for the spanwise direction (Figs. 8b and 9b). More specifically, the probability density function (PDF) for the base pressure gradient in the spanwise direction is centered about zero for both setups. There is one noticeable difference in the spanwise base pressure gradient PDF between both setups. The cavity

variant of the NDP exhibits a spanwise base pressure gradient PDF that is wider about the zero point (Fig. 9b). This goes along with the cavity variant rear wake's larger exploration of the vehicle base in the vertical direction. It is possible to conclusively say that the cavity appendage allows the rear wake to move more freely about the vehicle's rear base than is the case with the "squareback" NDP variant by analyzing the joint PDF of the base pressure gradients for both configurations (Fig. 10).

In total, the above base pressure gradient analysis does not permit the conclusive identification or exclusion of wake bimodality, particularly in the vertical direction. The simulated time is just not long enough (Figs. 8 and 9). From the collected data, it is possible to extract a time-averaged contour plot of pressure that depicts the strong wake asymmetry in the vertical direction for both flow configurations (Fig. 11). Meanwhile, instantaneous flow field snapshots from the collected data illustrate how the rear wake for both the "squareback" and cavity variant of the NDP rapidly explores asymmetric states in the spanwise direction (Figs. 12, 13).

After analyzing base pressure gradient plots and their associated wake tilts by looking at pressure contour plots, POD modal analysis is subsequently performed to obtain a more grounded understanding of the coherent flow structures that underlie these identified wake tilts. Figure 14 illustrates the third POD mode that was computed from flow field snapshots taken on the  $x_1x_3$ —middle plane passing through the two NDP configurations. Meanwhile, Fig. 15 depicts the second POD mode obtained from flow field snapshots taken on the  $x_1x_2$ —middle plane that goes through the two NDP variants. It is important to note that the energy for these computed POD modes on both planes is very distributed. At the very most, the first and, therefore, most energetic mode, possesses approximately 10% of the flow energy; it does not present any clean clearly discernible coherent flow structure though. The subsequent modes, namely two and three, possess between 3% and 6% of the flow's total energy. Such highly distributed flow energy content appears to indicate that, based on flow energy content, there is no dominating flow structure. However, one can still attempt to identify what the coherent structures represent.

In Fig. 14, one can discern a symmetric vortex shedding pattern in the spanwise plane. This is the case for both the "squareback" NDP (Fig. 14a) as well as the cavity variant of the NDP (Fig. 14b). Such a pattern is in stark contrast to the asymmetric rear vortex shedding modes in the spanwise direction that were detected as two distinct separate modes for the Ahmed body in Hesse and Morgans (2021). In Hesse and Morgans (2021), these

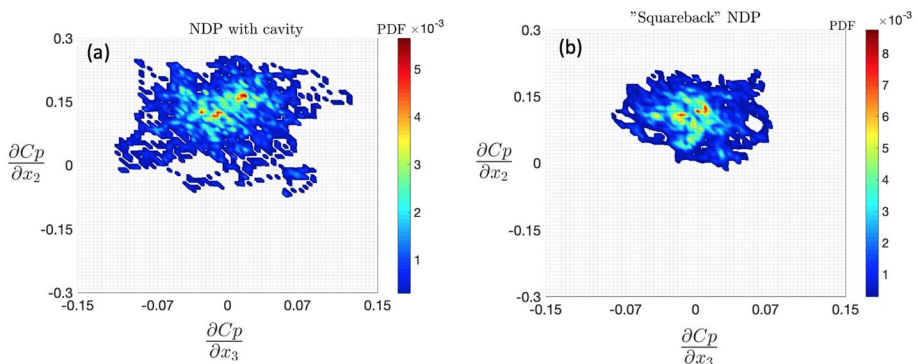


**Fig. 10** Joint PDF of base pressure gradients for **a** Nissan NDP with cavity and **b** the "squareback" NDP

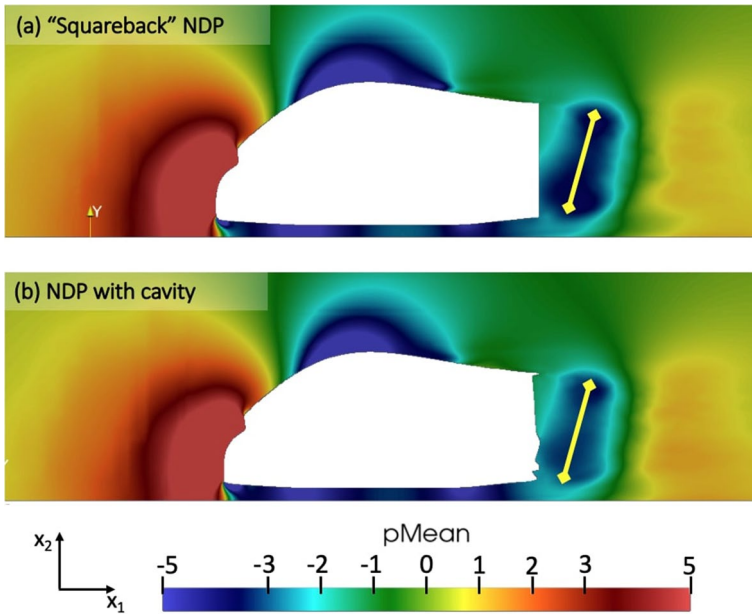


**Fig. 11** Mean pressure field snapshots highlighting the prominent wake asymmetry in the vertical direction for **a** the “squareback” NDP and **b** the NDP with a cavity at the rear

asymmetric rear vortex shedding modes in the spanwise direction for the Ahmed body were noted down as an immediate consequence of the rear wake spending longer periods of time in two opposite off-axis spanwise positions, and the associated bimodal wake switching events. As a result, the presented evidence for the two NDP geometry configurations appears to suggest that no wake bimodality in the spanwise direction will happen.

Additionally, Fig. 15 clearly depicts a highly asymmetric rear vortex shedding pattern in the top-to-bottom vertical plane for both the “squareback” and cavity variant of the NDP. Considering the previously noted evidence for wake bimodality in the spanwise direction for the Ahmed body, the current modal evidence suggests that it is possible to simulate and capture wake bimodality in the vertical direction for both configurations of the Nissan NDP. As the study by Dalla Longa et al. (2019) of a simplified lorry geometry and the study by Bonnavion et al. (2017) of the commercial Renault Kangoo illustrate, geometric vertical asymmetry introduced into the setup by the ground’s proximity and the vehicle shape’s vertical asymmetry does not preclude the occurrence of vertical wake bimodality for a vertically asymmetric wake. To conclusively validate this claim for the Nissan NDP, one must extend the currently presented non-dimensional simulation time-span,  $t^*$ , by an order of magnitude (Figs. 8 and 9) (Grandemange et al. 2013b).

Having identified and obtained an understanding of the flow structures present in the rear wake of the “squareback” and cavity variant of the NDP, their influence on integral flow quantities,  $C_D$  and  $C_L$ , is subsequently assessed. Both the time-average of the signal and root-mean-square (RMS) of the signals’ fluctuations are depicted in Table 2. Table 2 also presents the percentage delta of these quantities when comparing the “squareback” and cavity configuration of the NDP.

For one, it may be observed that the immediate impact of the cavity is to lower the absolute drag value. This supports the work done by Lucas et al. (2017), who, through

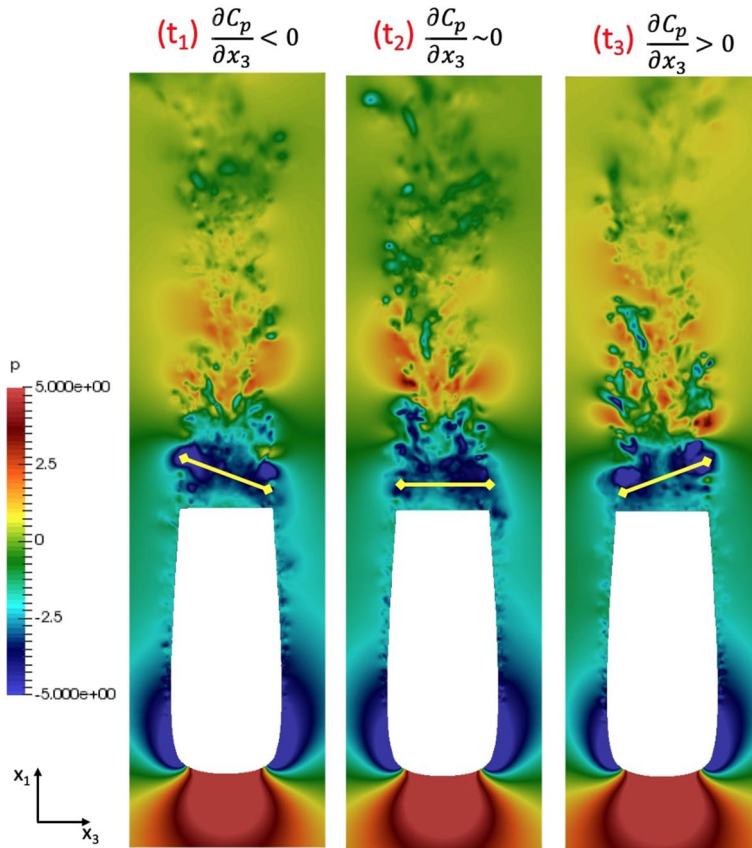


**Fig. 12** Pressure field snapshots highlighting short-lived moments of wake asymmetry in the spanwise direction for the “squareback” NDP. Times at which flow field snapshots are taken may be found in Fig. 8. The height of the plane lies at  $x_2 = G + 0.5H$

appending cavities to the canonical squareback Ahmed body, achieved drag reductions somewhere between 3% and 9.5%. In the current study on the Nissan NDP, drag is reduced by 13.6%, which illustrates that the cavity appendage is a beneficial passive flow control device. To understand the source of this drag reduction, Fig. 16 depicts the mean velocity field’s magnitude and its line integral convolution, while Fig. 17 illustrates the turbulent kinetic energy for both vehicle configurations. The TKE for the “squareback” variant has a larger magnitude in the immediate wake region compared to the cavity variant. Associated with this higher TKE is more flow mixing between the faster moving outer fluid shear layer of the wake and slower moving recirculating air-flow in the core of the wake, thereby re-energizing the wake flow. As a result, the saddle point of the wake, which is taken to be the end of the wake, for the “squareback” variant should be positioned further from the base of the vehicle than for the cavity variant. The plot of mean velocity magnitude (Fig. 16) shows that this is, in fact, not the case: the recirculation bubble length,  $L_B$ , of the “squareback” variant’s wake flow field is actually about 1.6% shorter than the cavity variant’s. As the work from Dalla Longa et al. (2017) shows, an increase in  $L_B$  should correlate with a reduction in mean drag. This



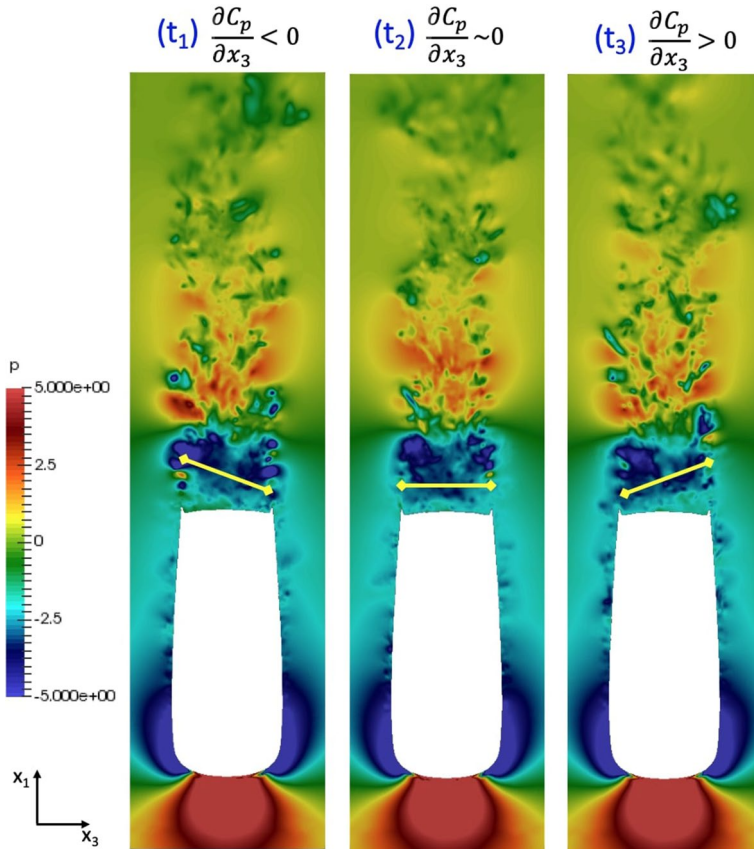
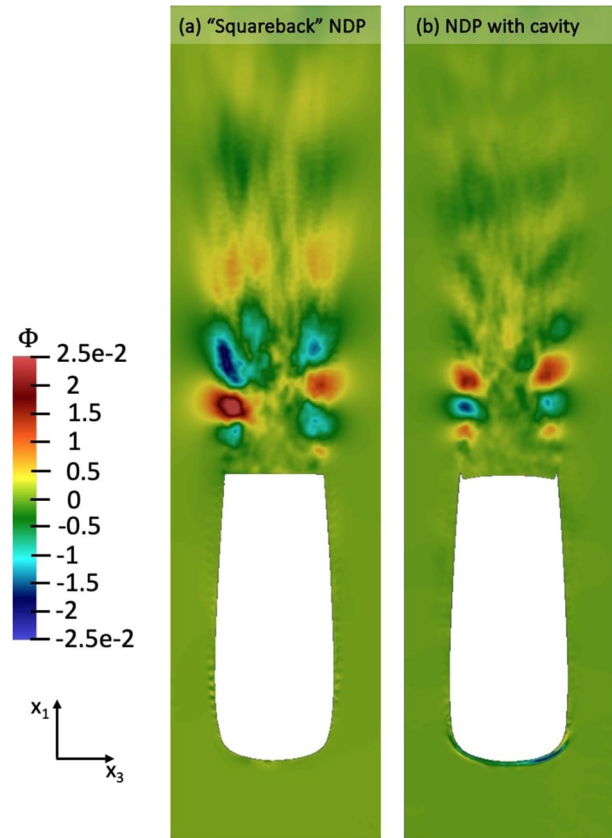


**Fig. 13** Pressure field snapshots highlighting short-lived moments of wake asymmetry in the spanwise direction for the NDP with cavity. Times at which flow field snapshots are taken may be found in Fig. 9. The height of the plane lies at  $x_2 = G + 0.5H$

lengthened recirculation bubble for the cavity variant is, thus, one possible reason for its lower drag value. However, it is insufficient to account for the 13.6% drag reduction of the cavity variant. As the mean pressure flow field (Fig. 11) and mean velocity field magnitude (Fig. 16) do not show too much deviation between the “squareback” and cavity variant, a further source of the cavity variant’s lower drag must be identified. This is done by looking at the cavity’s geometry. The cavity acts as a very short boat-tail, which reduces the amount of rear base surface area that the low pressure wake region acts upon. To be specific, there is a 5% reduction in rear base area due to the tapered cavity. It is this geometric feature brought on by the presence of the tapered cavity that is believed to play the larger role in the cavity variant’s mean drag reduction over the “squareback” variant.

Additionally, equally noteworthy is the cavity’s influence on the RMS values for both drag and lift. Specifically, the cavity reduces the RMS value of drag,  $C_D^2$ , by 68.7%, while it lowers the RMS value of lift,  $C_L^2$ , by 32.7%, respectively. These results show that the cavity reduces the flow field fluctuations around the Nissan NDP. This should translate to improved ride comfort, as, for instance, roadway noise should be less.

**Fig. 14** Symmetric vortex shedding in the spanwise direction visualized through the application of POD on instantaneous pressure data taken from the  $x_1x_3$ —middle plane that lies at  $x_2 = G + 0.5H$  for **a** the “squareback” NDP and **b** the NDP with a rear cavity. This is the third POD mode



Unfortunately, by appending a cavity to the Nissan NDP, the lift coefficient goes up in value. Such a reduction in downforce will lead to less cornering stability when the vehicle traverses corners at high speed. Fortunately, high speed cornering is typically not a key performance indicator (KPI) for vans like the Nissan NDP.

Furthermore, due to the failure to achieve truly converged values of lift and drag, as seen in the mesh refinement study of Sect. 2.5, one cannot take these percentage differences between the cavity and “squareback” variant of the Nissan NDP as absolute. Rather, one must accept that there is some inherent margin of error. Based on the mesh refinement study of Sect. 2.5, this margin of error lies at about 3% for drag and 10% for lift (see Table 1). Armed with this information, one can see that the margin of error for lift is in fact larger than its computed percentage delta between the “squareback” and cavity variant of the Nissan NDP. This reinforces the statement that lift variation in CFD can be quite high, as encountered in the work by Ashton et al. (2016).

### 3.2 Stationary Versus Moving Ground

This section is more qualitative. It analyzes, through visualization of the flow field, the implication of a moving ground when it comes to vehicle development. To achieve this, a comparison is performed between a stationary ground simulation and a moving ground

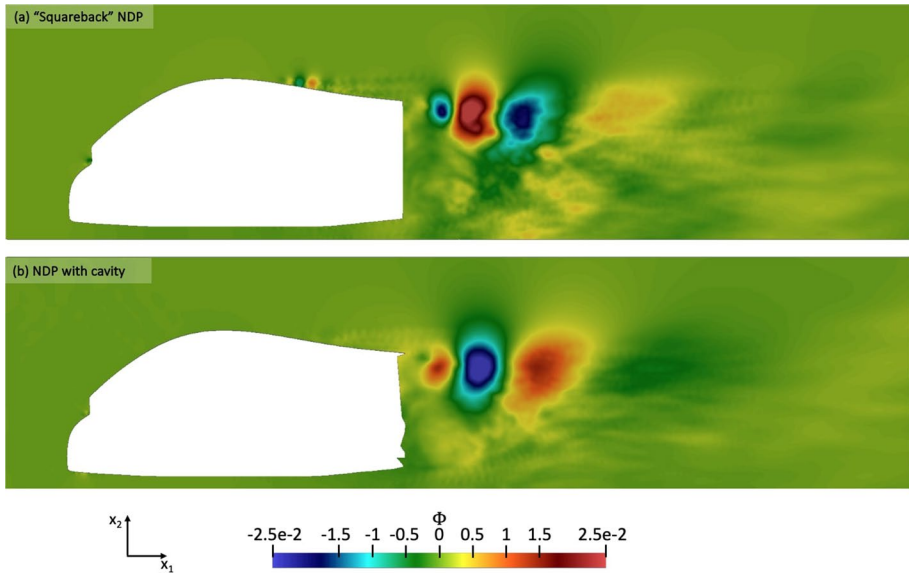


**Fig. 15** Asymmetric vortex shedding in the vertical direction visualized through the application of POD on instantaneous pressure data taken from the  $x_1x_2$ —middle plane for **a** the “squareback” NDP and **b** the NDP with a rear cavity. This is the second POD mode

simulation of the cavity variant of the Nissan NDP. Figures 18, 20, and 21 portray the instantaneous pressure field,  $x_3$ -vorticity field, and velocity magnitude field around the Nissan NDP, respectively, for both setups. Associated with these instantaneous flow field snapshots are videos that may be found in this paper’s supplementary material; they offer a further dimension to the analysis. Meanwhile, Figs. 19 and 22 depict the time-averaged pressure and velocity magnitude field, respectively, for both set-ups under consideration.

All flow field representations illustrate the detachment of a powerful vortex from the roof of the vehicle. In Sect. 3.1, this structure was alluded to. More specifically, it was postulated that this powerful vortex detachment is a reason for/contributor to the wake’s prominent vertical tilt away from the NDP’s top trailing edge. As was done for the vortex shedding mode in Sect. 3.1, it is possible to isolate and, thereby, visualize more clearly this coherent structure by applying the POD post-processing technique to the flow field data. The performed POD analysis suggests that the shed hairpin vortex structure contains approximately 3.5% of the system’s total energy. It is, thus, in this highly energy distributed system the fourth most energetic mode. Furthermore, this structure’s stationary ground and moving ground manifestation is essentially indistinguishable (Fig. 23).

Meanwhile, the aforementioned representations of the flow field around the Nissan NDP (Figs. 18, 19, 20, 21 and 22) underline the presence of a stationary ground in the simulation by exhibiting clockwise rotating (when looking into the page of the vertical plane) low pressure cores brought on by the fluid’s deceleration near the ground just aft of the vehicle base. The fluid’s deceleration is due to the no-slip boundary condition at the ground coupled to the the air flow progressing from an area of low pressure to one of higher pressure as it flows downstream of the vehicle under-body toward the wake’s far-field region.

Additionally, by visualizing iso-contours of  $Q^* = 59.8$  that are coloured by velocity magnitude (Fig. 24), one is able to depict vortex structures surrounding the vehicle.

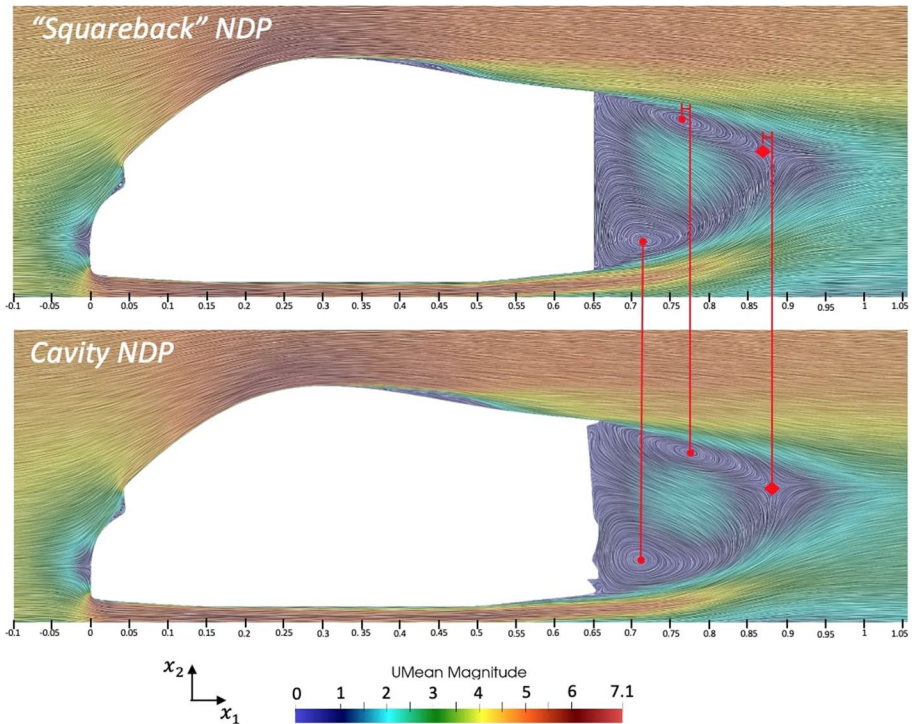


**Fig. 16** Comparison of the mean velocity field magnitude with LIC for the “squareback” and cavity variant of the NDP

Figure 24 does appear to show that the moving ground simulation drags the wake vortex structures further downstream than in the case of the stationary ground simulation. However, upon looking at the associated Q-criterion video that is appended as supplementary material, this is just a snap-shot occurrence. In general, the wake vortex structures are dragged away from the vehicle base to a similar extent in both the moving ground and stationary ground simulation. The apparent lack of difference between the moving ground and stationary ground set-up’s wake region is further evidenced by the mean pressure field (Fig. 19) and mean velocity field magnitude (Fig. 22) images, which are almost indistinguishable. Through these images one can see that the recirculation bubble length between both ground boundary condition set-ups is essentially the same and lies at approximately  $0.75 H$  (Table 1).

Despite this similarity between the wake regions of both set-ups, there is a 3.3% reduction in the time-averaged drag coefficient for the moving ground set-up over the stationary ground variant. For the stationary ground simulation, the value lies at 0.274, while in the case of the moving ground simulation, the drag value rests at 0.265 (Table 3). The augmented drag value for the stationary ground variant must be due to the presence of low pressure clockwise rotating (when looking into the page of the vertical plane) vortices near the ground brought on by the flow deceleration just aft of the vehicle base (Figs. 18, 19, 20, 21 and 22), as was described earlier.

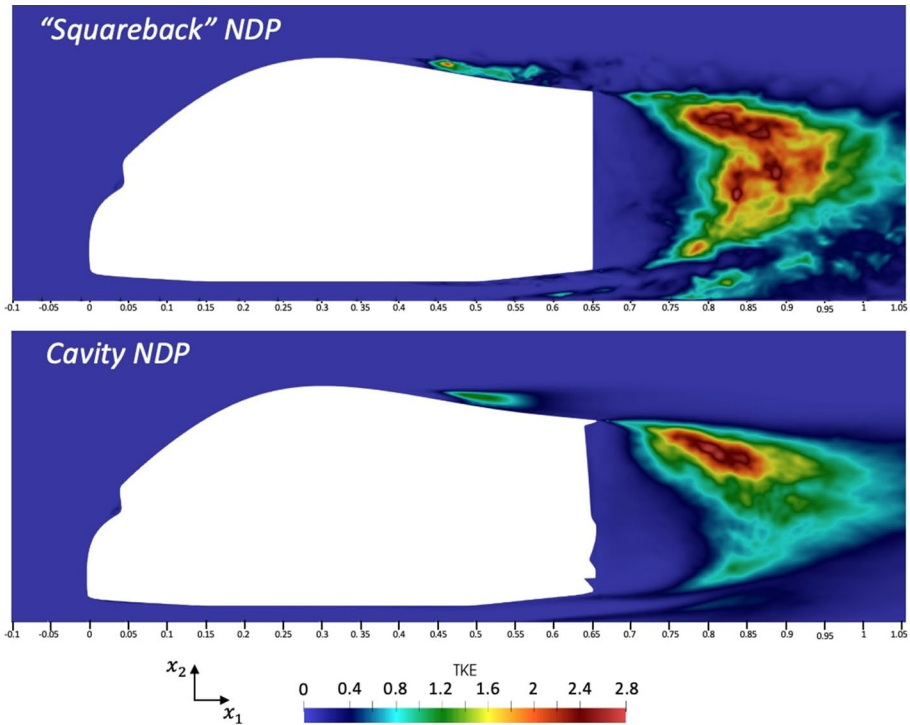


**Fig. 17** Comparison of the turbulent kinetic energy (TKE) for the “squareback” and cavity variant of the NDP

**Table 2** Integral flow quantities for the “squareback” NDP and NDP with a rear cavity

NDP Set-up	$\overline{C_D}$	% $\Delta$	$\overline{C_D'^2}$	% $\Delta$	$\overline{C_L}$	% $\Delta$	$\overline{C_L'^2}$	% $\Delta$
“Squareback”	0.317	–	0.0163	–	–0.0815	–	0.0107	–
Cavity	0.274	–13.6	0.0051	–68.7	–0.0750	8.0	0.0072	–32.7

By right, a moving ground simulation is more representative of real-world driving conditions, as a boundary layer should not be developing at the ground. However, with no reference data available, an absolute assessment cannot be made about whether the presented moving ground simulation better replicates the vehicle performance, such as the drag coefficient, of an on-road vehicle. In the current study, it is clear that the stationary ground simulation provides a more conservative design platform when considering the vehicle’s aerodynamics and designing the vehicle entirely virtually where there is no physical model for validation. By over-design, one makes sure that the drag coefficient target is met. It is not absolute though; a moving ground simulation does not invariably return a lower drag value than its fixed ground counterpart. This depends very strongly on several factors: is the vehicle underbody smooth or detailed, is one simulating tire behavior as well, and/or are side mirrors present. Heft et al. (2012) nicely illustrated this dependency of the moving ground drag value when releasing the open-source DrivAer model.



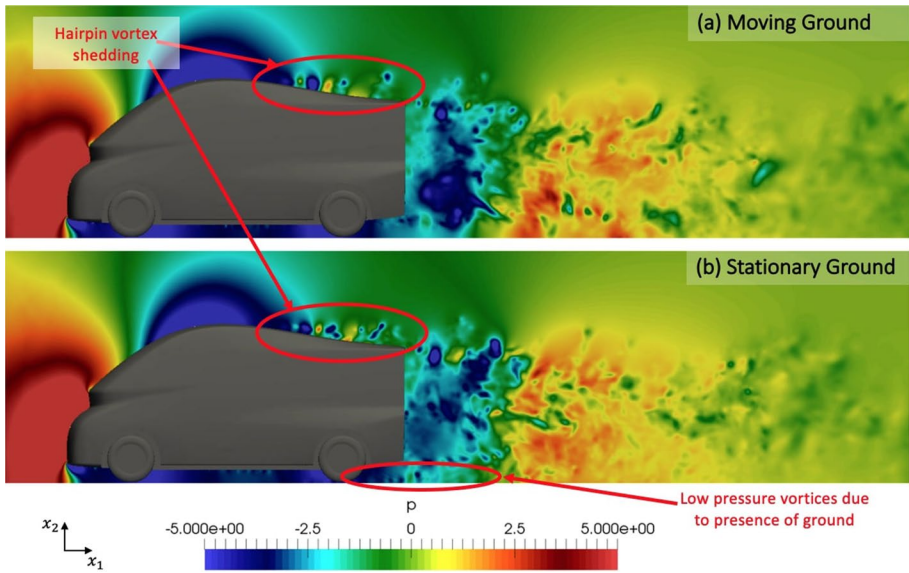


**Fig. 18** Instantaneous pressure flow field for **a** moving ground and **b** stationary ground simulation of the Nissan NDP with a rear cavity. An animation of this content can be found in the video “Pressure”

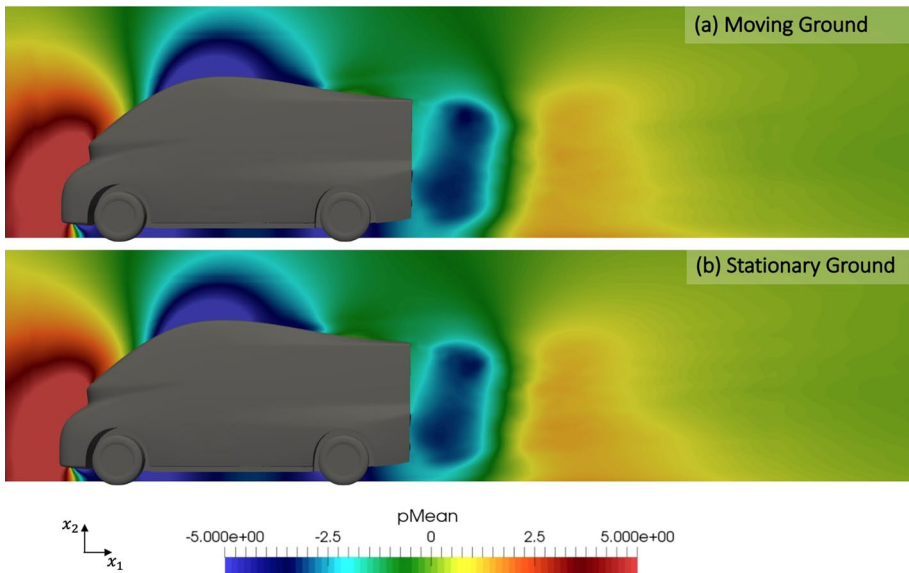


**Fig. 19** Average pressure flow field for **a** moving ground and **b** stationary ground simulation of the Nissan NDP with a rear cavity

The remaining integral flow quantities for the two considered simulations are subsequently analyzed. Specifically, the influence of a moving ground in the simulation is to accelerate the air flow under the Nissan NDP’s body and, thereby, reduce the lift value,



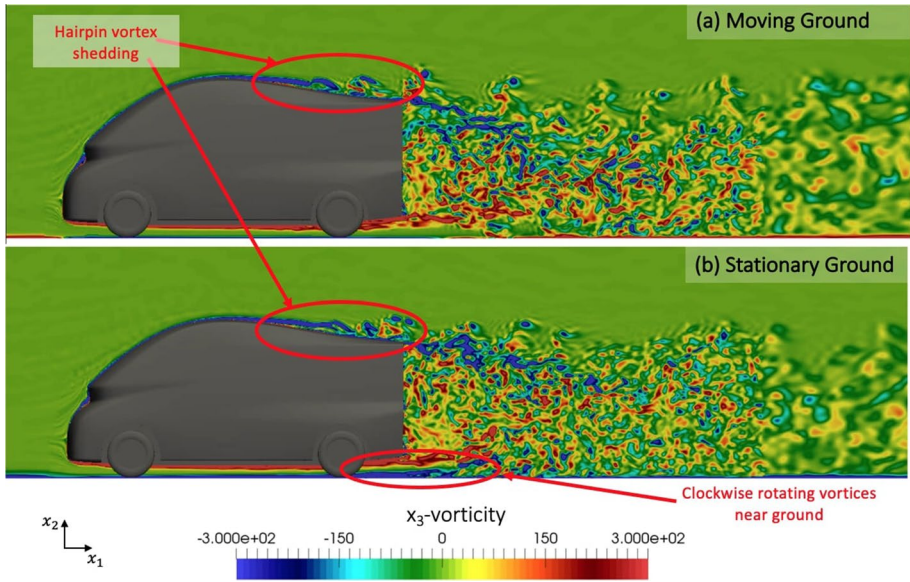


**Fig. 20** Instantaneous  $x_3$ -vorticity for **a** moving ground and **b** stationary ground simulation of the Nissan NDP with a rear cavity. An animation of this content can be found in the video “x3Vorticity”

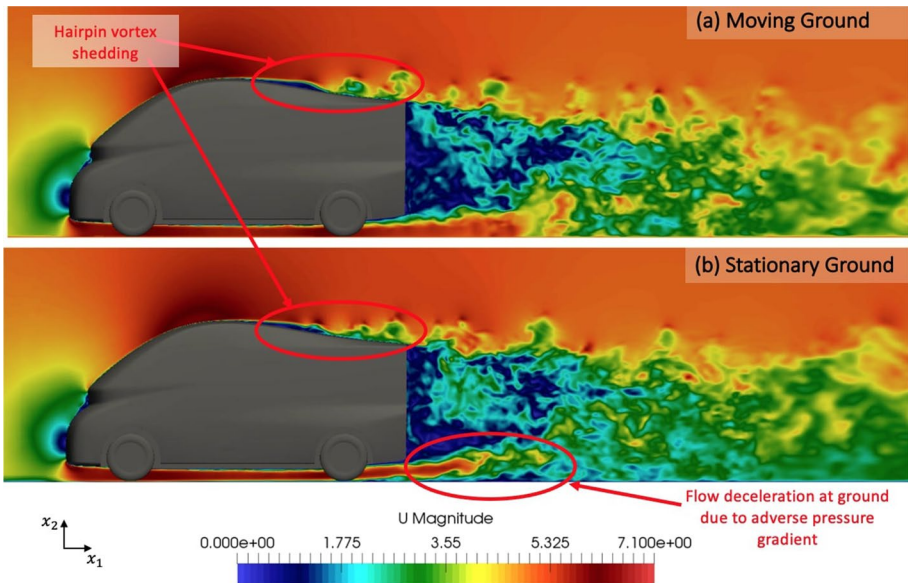


**Fig. 21** Instantaneous velocity magnitude field for **a** moving ground and **b** stationary ground simulation of the Nissan NDP with a rear cavity. An animation of this content can be found in the video “VelocityMagnitude”

generating more downforce. For the moving ground simulation, lift lies at  $-0.089$  while for the stationary ground simulation the value rests at  $-0.075$  (Table 3). Meanwhile, RMS

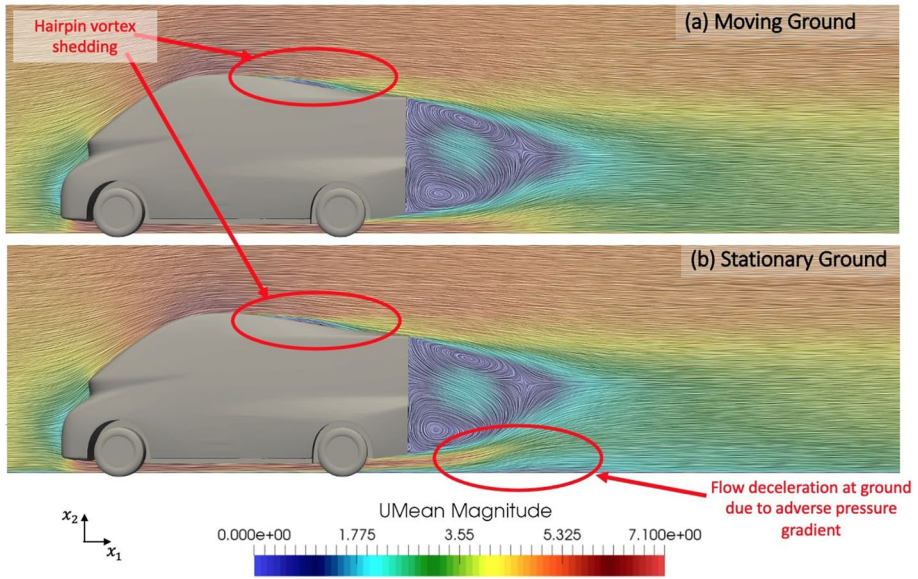


**Fig. 22** Mean velocity magnitude field with LIC for **a** moving ground and **b** stationary ground simulation of the Nissan NDP with a rear cavity

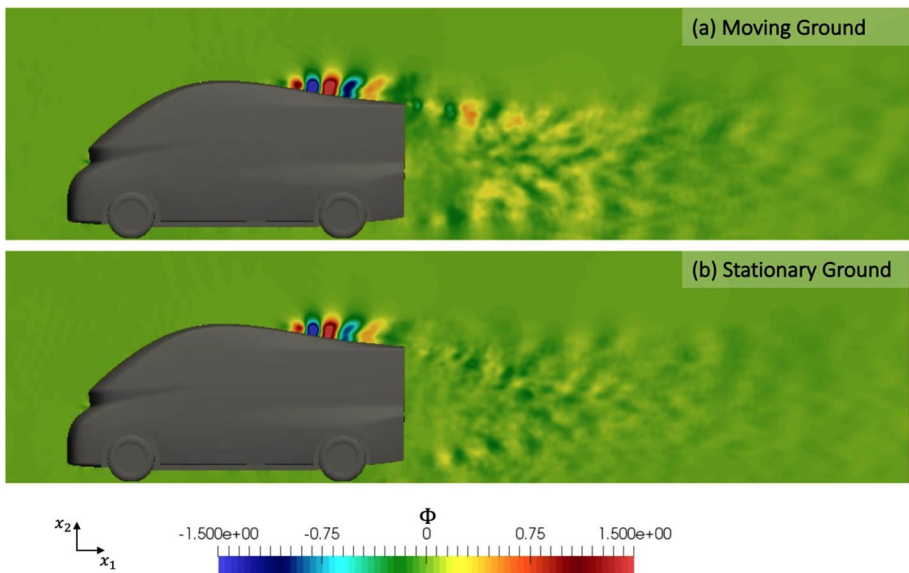


**Fig. 23** Roof hairpin vortex visualized through the application of POD on instantaneous pressure data taken from the  $x_1, x_2$ —middle plane for **a** moving ground and **b** stationary ground simulation of the Nissan NDP with a rear cavity. This is the fourth POD mode

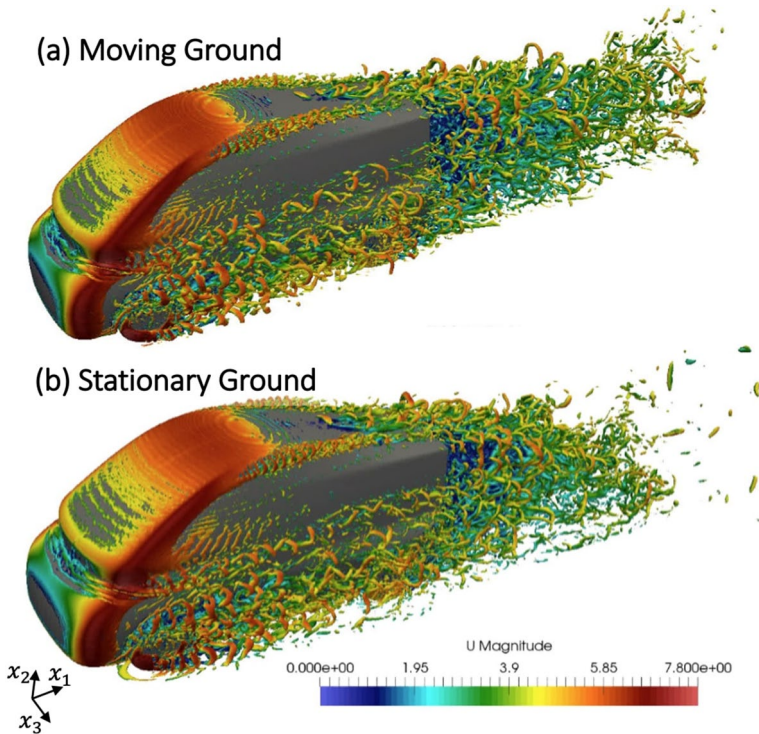


**Fig. 24** Vortex structure visualization through  $Q^*$  criterion iso-contours of  $Q^* = 59.8$  for **a** moving ground and **b** stationary ground simulation of the Nissan NDP with a rear cavity. An animation of this content can be found in the video “QCriterion”

**Table 3** Integral flow quantities for the stationary ground and moving ground simulation of the NDP with a rear cavity

Ground Set-up	$\overline{C_D}$	% $\Delta$	$\overline{C_D^2}$	% $\Delta$	$\overline{C_L}$	% $\Delta$	$\overline{C_L^2}$	% $\Delta$
Stationary	0.274	–	0.0051	–	– 0.075	–	0.0072	–
Moving	0.265	– 3.3	0.0064	25.5	– 0.089	– 18.7	0.0060	– 16.7

values of drag and lift for the two simulation set-ups look rather inconclusive. This is because for drag the RMS increases, while for lift the RMS decreases, both by comparable amounts, between the fixed ground and moving ground simulation (Table 3).

### 4 Conclusion

A  $Re_H = 100,000$  flow past the 15% scale model of the Nissan NDP is simulated using WRLES. Two comparisons are performed. The first analyzes rear wake asymmetries as part of a preliminary analysis that focuses on the possible presence of wake bimodality: the

comparison looks at the flow fields aft of a “squareback” and cavity variant of the NDP. It is determined that no wake bimodality in the spanwise direction is likely to occur: there is no long-term spanwise wake asymmetry and POD indicates that trailing edge vortex shedding is symmetric in the spanwise plane. However, there is the possibility that wake bimodality in the vertical direction is present: there is a prominent vertical tilt of the wake and asymmetric vortex shedding in this plane. To conclusively determine this, the non-dimensional simulation duration,  $t^*$ , must be extended by at least an order of magnitude though. The immediate effect of the cavity is to release the rear wake from its more restricted motion that is present with the “squareback” variant. This, coupled to a 5% reduction in rear base area for the cavity NDP over its “squareback” variant, reduces the drag value by 13.6%, illustrating that the cavity is a powerful passive flow control device. The second comparison involves the use of a moving ground simulation as compared to a stationary ground simulation for the Nissan NDP with a cavity. It is found that having a fixed ground is associated with the presence of low pressure clockwise rotating (when looking into the page of the vertical plane) vortices near the ground brought on by the flow deceleration just aft of the vehicle base. This translates to a 3.3% higher drag value prediction with a stationary ground compared to the moving ground set-up. As such, although the moving ground should better replicate the real-world driving scenario, it is the stationary ground variant that allows the incorporation of a more conservative aerodynamic design strategy when conceptualizing the NDP vehicle solely in the virtual domain using a digital twin.

**Supplementary Information** The online version contains supplementary material available at <https://doi.org/10.1007/s10494-023-00400-x>.

**Acknowledgements** The authors would like to thank Siemens PLM for providing a Star-CCM+ license and user-support where needed, as well as Nissan for providing the NDP CAD files. Financial support from the Engineering and Physical Sciences Research Council (EPSRC) and Nissan is also greatly appreciated. This work benefited immensely from computational power provided by the Imperial College of London HPC cluster, CX2. It also benefited from computing resources made available through the UK Turbulence Consortium using the UK’s leading computing facility, ARCHER and subsequently ARCHER2.

**Author Contributions** Faron Hesse and Aimee S. Morgans wrote the main manuscript text and prepared all figures. All authors reviewed the manuscript as well.

**Funding** The work reported in this paper was supported by funding from the Engineering and Physical Sciences Research Council as well as by funding from the Nissan Motor Company.

## Declarations

**Conflict of interest** I declare that the authors have no competing interests as defined by Springer, or other interests that might be perceived to influence the results and/or discussion reported in this paper.

**Ethical Approval** I confirm that the authors have upheld the integrity of the scientific record, thereby complying with the journal’s ethics policy.

**Informed Consent** I confirm that all of the material is owned by the authors and/or no permissions from third parties are required.

**Open Access** This article is licensed under a Creative Commons Attribution 4.0 International License, which permits use, sharing, adaptation, distribution and reproduction in any medium or format, as long as you give appropriate credit to the original author(s) and the source, provide a link to the Creative Commons licence, and indicate if changes were made. The images or other third party material in this article are included in the article’s Creative Commons licence, unless indicated otherwise in a credit line to the material. If material is not included in the article’s Creative Commons licence and your intended use is not



permitted by statutory regulation or exceeds the permitted use, you will need to obtain permission directly from the copyright holder. To view a copy of this licence, visit <http://creativecommons.org/licenses/by/4.0/>.

## References

- Ahmed, S.R., Ramm, G., Faltin, G.: Some salient features of the time-averaged ground vehicle wake. SAE Technical Paper Series 840300 (1984)
- Ahmed, S.R.: Wake structure of typical automobile shapes. *J. Fluids Eng.* **103**, 162–169 (1981)
- Alajbegovic, A., Lew, P., Shock, R., Duncan, B., Hoch, J.: Aerodynamic simulation of a standalone rotating tread tire. *Int. J. Autom. Eng.* **8**, 171–178 (2017)
- Aljure, D.E., Calafell, J., Baez, A., Oliva, A.: Flow over a realistic car model: wall modeled large eddy simulations assessment and unsteady effects. *J. Wind Eng. Ind. Aerodyn.* **174**, 225–240 (2018)
- Ambrose, S., Morvan, H., Simmons, K.: Investigation of oil jet impingement on a rotating gear using lattice Boltzman method (LBM). In: Turbo Expo: Power for Land, Sea, and Air, American Society of Mechanical Engineers. p. V001T01A028 (2018)
- Ashton, N., West, A., Lardeau, S., Revell, A.: Assessment of RANS and DES methods for realistic automotive models. *Comput. Fluids* **128**, 1–15 (2016)
- Barton, I.E.: Comparison of SIMPLE- and PISO-type algorithms for transient flows. *Int. J. Numer. Methods Fluids* **26**, 459–483 (1998)
- Bearman, P.W.: Near wake flows behind two-and three-dimensional bluff bodies. *J. Wind Eng. Ind. Aerodyn.* **69**, 33–54 (1997)
- Bonnayon, G., Cadot, O., Évrard, A., Herbert, V., Parpais, S., Vigneron, R., Détery, J.: On multistabilities of real car's wake. *J. Wind Eng. Ind. Aerodyn.* **164**, 22–33 (2017)
- Bonnayon, G., Cadot, O., Herbert, V., Parpais, S., Vigneron, R., Détery, J.: Asymmetry and global instability of real minivans' wake. *J. Wind Eng. Ind. Aerodyn.* **184**, 77–89 (2019)
- Brackston, R.D., García de la Cruz, J., Wynn, A., Rigas, G., Morrison, J.F.: Stochastic modelling and feedback control of bistability in a turbulent bluff body wake. *J. Fluid Mech.* **802**, 726–749 (2016)
- Charpentier, A., Hwang, Y., Noh, J., Caro, S.: Validation of fuel tank slosh noise and vibration predictions. In: INTER-NOISE and NOISE-CON Congress and Conference Proceedings, Institute of Noise Control Engineering. pp. 2343–2353 (2016)
- Choi, H., Moin, P.: Grid-point requirements for large eddy simulation: Chappans estimates revisited. *Phys. Fluids* **24**, 011702 (2012)
- Dalla Longa, L., Morgans, A.S., Dahan, J.A.: Reducing the pressure drag of a D-shaped bluff body using linear feedback control. *Theor. Comput. Fluid Dyn.* **31**, 567–577 (2017)
- Dalla Longa, L., Evstafyeva, O., Morgans, A.S.: Simulations of the bi-modal wake past three-dimensional blunt bluff bodies. *J. Fluid Mech.* **866**, 791–809 (2019)
- Edenhofer, O., Sokona, Y., Farahani, E., Kadner, S., Seyboth, K., Adler, A.: Climate Change 2014: Mitigation of Climate Change, 1st edn. Cambridge University Press, New York (2014)
- Évrard, A., Cadot, O., Herbert, V., Ricot, D., Vigneron, R., Détery, J.: Fluid force and symmetry breaking modes of a 3D bluff body with a base cavity. *J. Fluids Struct.* **61**, 99–114 (2016)
- Evstafyeva, O., Morgans, A.S., Dalla Longa, L.: Simulation and feedback control of the Ahmed body flow exhibiting symmetry breaking behaviour. *J. Fluid Mech.* **817**, R2 (2017)
- Fan, Y., Xia, C., Chu, S., Yang, Z., Cadot, O.: Experimental and numerical analysis of the bi-stable turbulent wake of a rectangular flat-backed bluff body. *Phys. Fluids* **32**, 105111 (2020)
- Gaylard, A.P., Jilesen, J., Duncan, B., Konstantinov, A., Wanderer, J.: Simulation of rear and body side vehicle soiling by road sprays using transient particle tracking. *SAE Int. J. Passeng. Cars Mech. Syst.* **6**, 424–435 (2013)
- Gaylard, A.P., Kabanovs, A., Jilesen, J., Kirwan, K., Lockerby, D.A.: Simulation of rear surface contamination for a simple bluff body. *J. Wind Eng. Ind. Aerodyn.* **165**, 13–22 (2017)
- Grandemange, M., Cadot, O., Gohlke, M.: Reflectional symmetry breaking of the separated flow over three-dimensional bluff bodies. *Phys. Rev. E* **86**, 035302 (2012)
- Grandemange, M., Gohlke, M., Cadot, O.: Bi-stability in the turbulent wake past parallelepiped bodies with various aspect ratios and wall effects. *Phys. Fluids* **25**, 095103 (2013)
- Grandemange, M., Gohlke, M., Cadot, O.: Turbulent wake past a three-dimensional blunt body. Part 1. Global modes and bi-stability. *J. Fluid Mech.* **722**, 51–84 (2013)
- Grandemange, M., Gohlke, M., Cadot, O.: Turbulent wake past a three-dimensional blunt body. Part 2. Experimental sensitivity analysis. *J. Fluid Mech.* **752**, 439–461 (2014)

- Guilmineau, E., Deng, G., Leroyer, A., Queutey, P., Visonneau, M., Wackers, J.: Assessment of hybrid RANS-LES formulations for flow simulation around the Ahmed body. *Comput. Fluids* **176**, 302–319 (2018)
- Han, T.: Computational analysis of three-dimensional turbulent flow around a bluff body in ground proximity. *AIAA J.* **27**, 1213–1219 (1989)
- He, P., Mader, C.A., Martins, J.R., Maki, K.J.: An aerodynamic design optimization framework using a discrete adjoint approach with OpenFOAM. *Comput. Fluids* **168**, 285–303 (2018)
- Heft, A., Indinger, T., Adams, N.A.: Introduction of a new realistic generic car model for aerodynamic investigations. SAE Technical Paper 2012-01-0168 (2012)
- Hesse, F.: Flow Control for Road Vehicle Drag Reduction. Ph.D. thesis. Imperial College London (2021)
- Hesse, F., Morgans, A.S.: Simulation of wake bimodality behind squareback bluff-bodies using LES. *Comput. Fluids* **223**, 104901 (2021)
- Howard, R.J.A., Pourquie, M.: Large eddy simulation of an Ahmed reference model. *J. Turbul.* **3**, 1–18 (2002)
- Hucho, W.H., Sovran, G.: Aerodynamics of road vehicles. *Ann. Rev. Fluid Mech.* **25**, 485–537 (1993)
- John, M., Buga, S.D., Monti, I., Kuthada, T., Wittmeier, F., Gray, M., Laurent, V.: Experimental and numerical study of the drivAer model aerodynamics. SAE International (2018)
- Kotapati, R., Keating, A., Kandasamy, S., Duncan, B., Shock, R., Chen, H.: The lattice-Boltzmann-VLES method for automotive fluid dynamics simulation, a review. SAE Technical Paper 2009-26-0057 (2009)
- Krajnović, S., Davidson, L.: Numerical study of the flow around a bus-shaped body. *J. Fluids Eng.* **125**, 500–509 (2003)
- Kremheller, A., LeGood, G., Annetts, I., Moore, M.: The aerodynamics development of a new light commercial vehicle concept under uniform and transient flow conditions. In: 10th FKFS Conference (2015)
- Kremheller, A., Moore, M., LeGood, G., Sims-Williams, D., Newborn, J., Lewis, R.: The effects of transient flow conditions on the aerodynamics of an LCV concept using CFD and wind tunnel experiments. In: International Conference on Vehicle Aerodynamics 2016 : Aerodynamics by Design, IMechE, Coventry, England (2016)
- Li, R., Barros, D., Borée, J., Cadot, O., Noack, B.R., Cordier, L.: Feedback control of bimodal wake dynamics. *Exp. Fluids* **57**, 158 (2016)
- Linuma, Y., Taniguchi, K., Oshima, M.: Aerodynamics development for a new EV hatchback considering crosswind sensitivity. SAE Technical Paper 2018-01-0715 (2018)
- Ljungskog, E., Sebben, S., Broniewicz, A.: Inclusion of the physical wind tunnel in vehicle CFD simulations for improved prediction quality. *J. Wind Eng. Ind. Aerodyn.* **197**, 104055 (2020)
- Lucas, J.M., Cadot, O., Herbert, V., Parpais, S., Détery, J.: A numerical investigation of the asymmetric wake mode of a squareback Ahmed body—effect of a base cavity. *J. Fluid Mech.* **831**, 675–697 (2017)
- Lumley, J.L.: The structure of inhomogeneous turbulent flows. *Atmos. Turbul. Radio Wave Propag.* (1967)
- Manceau, R., Bonnet, J.: Refined turbulence modelling. In: Proceedings of the 10th ERCOFTAC (SIG-15)/IAHR/QNET-CFD Workshop (2002)
- Nicoud, F., Ducros, F.: Subgrid-scale stress modelling based on the square of the velocity gradient tensor. *Flow Turbul. Combust.* **62**, 183–200 (1999)
- Othmer, C.: Adjoint methods for car aerodynamics. *J. Math. Ind.* **4**, 1–23 (2014)
- Papoutsis-Kiachagias, E.M., Asouti, V.G., Giannakoglou, K.C., Gkagkas, K., Shimokawa, S., Itakura, E.: Multi-point aerodynamic shape optimization of cars based on continuous adjoint. *Struct. Multidiscip. Optim.* **59**, 675–694 (2019)
- Pasquetti, R., Peres, N.: A penalty model of synthetic micro-jet actuator with application to the control of wake flows. *Comput. Fluids* **114**, 203–217 (2015)
- Patankar, S.V., Spalding, D.B.: Paper 5—A calculation procedure for heat, mass and momentum transfer in three-dimensional parabolic flows. *Numerical Prediction of Flow, Heat Transfer, Turbulence and Combustion*, pp. 54–73 (1972)
- Pavia, G., Passmore, M., Sardu, C.: Evolution of the bi-stable wake of a square-back automotive shape. *Exp. Fluids* **59**, 20 (2018)
- Perry, A.K., Pavia, G., Passmore, M.: Influence of short rear end tapers on the wake of a simplified square-back vehicle: wake topology and rear drag. *Exp. Fluids* **57**, 169 (2016)
- Piomelli, U.: Wall-layer models for large-eddy simulations. *Progress Aerosp. Sci.* **44**, 437–446 (2008)
- Piomelli, U., Balaras, E.: Wall-layer models for large-eddy simulations. *Ann. Rev. Fluid Mech.* **34**, 349–374 (2002)
- Podvin, B., Pellerin, S., Fraigneau, Y., Bonnavion, G., Cadot, O.: Low-order modelling of the wake dynamics of an Ahmed body. *J. Fluid Mech.* **927**, R6 (2021)



- Rao, A.N., Zhang, J., Minelli, G., Basara, B., Krajnović, S.: An LES investigation of the near-wake flow topology of a simplified heavy vehicle. *Flow Turbul. Combust.* 1–27 (2018b)
- Rao, A.N., Minelli, G., Zhang, J., Basara, B., Krajnović, S.: Investigation of the near-wake flow topology of a simplified heavy vehicle using PANS simulations. *J. Wind Eng. Ind. Aerodyn.* **183**, 243–272 (2018)
- Reynolds, W.C.: The potential and limitations of direct and large eddy simulations. In: *Whither Turbulence? Turbulence at the Crossroads*, pp. 313–343. Springer (1990)
- Rigas, G., Oxlade, A.R., Morgans, A.S., Morrison, J.F.: Low-dimensional dynamics of a turbulent axisymmetric wake. *J. Fluid Mech.* **755**, R5 (2014)
- Rigas, G., Morgans, A.S., Brackston, R.D., Morrison, J.F.: Diffusive dynamics and stochastic models of turbulent axisymmetric wakes. *J. Fluid Mech.* **778**, R2 (2015)
- Smagorinsky, J.: General circulation experiments with the primitive equations: the basic experiment. *Mon. Weather Rev.* **91**, 99–164 (1963)
- Spalart, P., Allmaras, S.: A one-equation turbulence model for aerodynamic flows. In: *30th Aerospace Sciences Meeting and Exhibit*, p. 439 (1992)
- Taira, K., Brunton, S.L., Dawson, S.T.M., Rowley, C.W., Colonius, T., McKeon, B.J., Schmidt, O.T., Gordeyev, S., Theofilis, V., Ukeiley, L.S.: Modal analysis of fluid flows: an overview. *AIAA J.* **55**, 4013–4041 (2017)
- Tennekes, H., Lumley, J.L., Lumley, J.L.: *A First Course in Turbulence*. MIT Press, Cambridge (1972)
- Versteeg, H.K., Malalasekera, W.: *An Introduction to Computational Fluid Dynamics: The Finite, vol. method*. Pearson Education, London (2007)

## Authors and Affiliations

Faron Hesse<sup>1</sup> · Aimee S. Morgans<sup>1</sup>

✉ Faron Hesse  
faronhesse@gmail.com

<sup>1</sup> Department of Mechanical Engineering, Imperial College London, London SW7 2AZ, UK